The Cyclonic Mode of Arctic Ocean Circulation

JAMES MORISON,[a] RON KWOK,[a] SUZANNE DICKINSON,[a] ROGER ANDERSEN,[a] CECILIA PERALTA-FERRIZ,[a] DAVID MORISON,[b] IGNATIUS RIGOR,[a] SARAH DEWEY,[c] AND JOHN GUTHRIE[a]

[a] *Polar Science Center, University of Washington, Seattle, Washington*
[b] *University of Utah, Salt Lake, Utah*
[c] *Kennedy School, Harvard University, Cambridge, Massachusetts*

(Manuscript received 13 August 2020, in final form 2 December 2020)

ABSTRACT: Arctic Ocean surface circulation change should not be viewed as the strength of the anticyclonic Beaufort Gyre. While the Beaufort Gyre is a dominant feature of average Arctic Ocean surface circulation, empirical orthogonal function analysis of dynamic height (1950–89) and satellite altimetry–derived dynamic ocean topography (2004–19) show the primary pattern of variability in its cyclonic mode is dominated by a depression of the sea surface and cyclonic surface circulation on the Russian side of the Arctic Ocean. Changes in surface circulation after Arctic Oscillation (AO) maxima in 1989 and 2007–08 and after an AO minimum in 2010 indicate the cyclonic mode is forced by the AO with a lag of about 1 year. Associated with a one standard deviation increase in the average AO starting in the early 1990s, Arctic Ocean surface circulation underwent a cyclonic shift evidenced by increased spatial-average vorticity. Under increased AO, the cyclonic mode complex also includes increased export of sea ice and near-surface freshwater, a changed path of Eurasian runoff, a freshened Beaufort Sea, and weakened cold halocline layer that insulates sea ice from Atlantic water heat, an impact compounded by increased Atlantic Water inflow and cyclonic circulation at depth. The cyclonic mode's connection with the AO is important because the AO is a major global scale climate index predicted to increase with global warming. Given the present bias in concentration of in situ measurements in the Beaufort Gyre and Transpolar Drift, a coordinated effort should be made to better observe the cyclonic mode.

KEYWORDS: Ocean; Arctic; Arctic Oscillation; Currents; Ekman pumping/transport; Ocean circulation

1. Introduction

Present Arctic Ocean near-surface circulation is commonly characterized as being in an anticyclonic phase (Hofmann et al. 2015; McPhee et al. 2009; Proshutinsky et al. 2015, 2009). This idea is largely based on in situ observations in the Canada Basin that are biased toward measuring the intensity of the anticyclonic Beaufort Gyre and on a regional index of Arctic Ocean circulation, the Arctic Ocean Oscillation index (AOOI). The AOOI is the sea surface height gradient across the Beaufort Gyre simulated with a wind-driven barotropic model (Proshutinsky and Johnson 1997; Proshutinsky et al. 2015). When the gradient (AOOI) is larger than average the ocean is said to be in an anticyclonic regime, and when the gradient is less than average the ocean is said to be in a cyclonic regime. The freshwater argument is that under a strengthening Beaufort high in atmospheric pressure, increased anticyclonic surface stress results in Ekman transport convergence of relatively fresh near surface water associated with ice melt, elevated sea surface height at the center of the gyre, increased anticyclonic surface geostrophic current, and increased freshwater content in the Beaufort Gyre and Arctic Ocean as a whole (Giles et al. 2012; McPhee et al. 2009; Proshutinsky et al. 2009).

However, intensification of the Beaufort Gyre does not necessarily mean the Arctic Ocean as a whole is in an anticyclonic regime. In fact, the Arctic Ocean near-surface circulation became more cyclonic in the early 1990s, even while freshwater content increased in the Beaufort Gyre. Hydrographic measurements in the early 1990s (Carmack et al. 1995, 1997; McLaughlin et al. 1996; Morison et al. 1998; Steele and Boyd 1998) indicate that the Transpolar Front between more saline Atlantic-derived and fresher Pacific-derived upper-ocean halocline waters had shifted toward Canada and Alaska. Earlier climatology (Gorshkov 1983; Treshnikov 1977) had the front over the Lomonosov Ridge. The difference between salinity measured by the submarine USS *Pargo* in 1993 (Fig. 1a) and the salinity of the 1950–89 summer climatology of the U.S.–Russian Arctic Ocean Atlas of the Environmental Working Group (EWG) (Timokhov and Tanis 1997b) (Fig. 1b; Morison et al. 2012) illustrates the cyclonic shift in the Transpolar Front to roughly over the Alpha and Mendeleyev ridges (Morison et al. 1998, 2000) with a 2-psu increase in salinity of the upper 200 m in the central Arctic Ocean and Makarov Basin (see Fig. 1a for place names). Cyclonic circulation in the Makarov Basin (Morison et al. 1998) was associated with this salinity increase and shift in the Transpolar Front.

Even while the 1993 data display a cyclonic shift in large-scale circulation characterized by increased salinity in the Makarov Basin and cyclonic shift in the Transpolar Front, the salinity anomaly in the Beaufort Sea freshened by 1–3 psu (Morison et al. 2012) suggesting an intensification of the anticyclonic Beaufort Gyre (Fig. 1b). The spatial pattern of increased

Denotes content that is immediately available upon publication as open access.

Corresponding author: James Morison, jhm2@uw.edu

DOI: 10.1175/JPO-D-20-0190.1

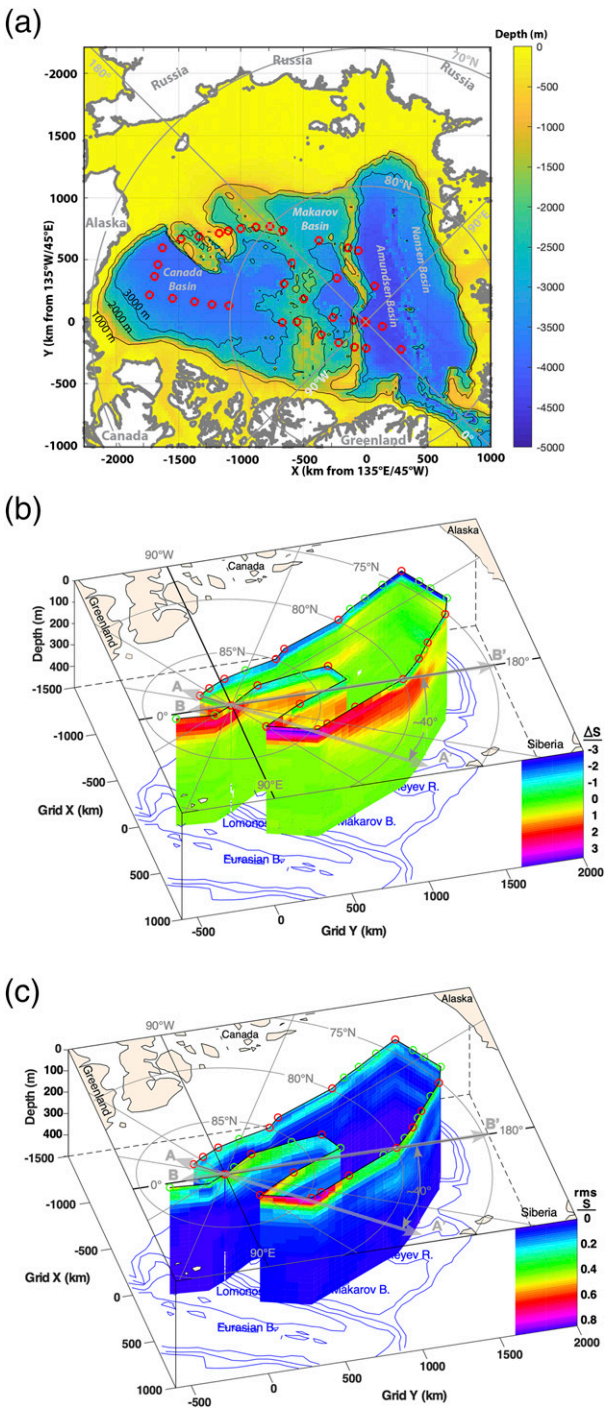

FIG. 1. (a) *Pargo* 1993 stations and Arctic Ocean bathymetry. (b) Perspective view of *Pargo* 1993 salinity anomaly relative to the 1950–89 summer climatology. Transpolar Front pre-1990 at A–A′, 1993 at B–B′, (c) RMS salinity variation in the 1970s from the EWG 1950–89 winter climatology. Panels (b) and (c) are adapted from Morison et al. (2012, Fig. S4).

upper-ocean salinity in the Makarov Basin and North Pole region and decreased upper-ocean salinity in the Beaufort Sea is similar to but a factor of about 5 times more intense than the pattern of 1970s root-mean-square (RMS) salinity variation (Fig. 1c; from Morison et al. 2012, their Fig. S4b) from U.S.–Russian climatology (Timokhov and Tanis 1997a). This suggests the 1993 anomalies were an extreme example of a fundamental mode of Arctic Ocean variability.

The ocean changes in the early 1990s extended to the deeper Atlantic Water boundary currents, specifically to an increase in Atlantic Water temperature (Carmack et al. 1997; Dickson et al. 2000; Morison et al. 2000; Swift et al. 1997). The 1993 *Pargo* data (Morison et al. 2000) show that over the Lomonosov Ridge, the Atlantic Water temperature maximum was 1°C greater than climatology, the temperature at 200 m was 2°C greater than climatology, and the temperature gradient to the surface was increased. Temperatures in the Makarov Basin in a layer centered at 200 m were increased 1°C due to the intrusion of Atlantic-derived halocline water. Swift et al. (1997) used observations from cruises in 1990 (Quadfasel et al. 1991), 1991 (Anderson et al. 1994; Rudels et al. 1994), and 1994 (Carmack et al. 1997; Swift et al. 1997) to trace Atlantic Water warming along the boundary currents of the Lomonosov Ridge and Eurasian Basin back to increased temperature of the Atlantic water inflow through Fram Strait starting at the end of the 1980s.

The 1993 pattern of change in near-surface circulation and Atlantic Water properties was observed after a record high in the wintertime Arctic Oscillation (AO) index in 1989 and 1990 three standard deviations above the previous (1950–88) average. The AO is the first empirical orthogonal function (EOF1) of atmospheric sea level pressure (SLP) north of 20°N, and an increase in the AO index indicates decreasing SLP over the eastern Arctic Ocean (Thompson and Wallace 1998, 2000; Thompson et al. 2000) and a strengthening of the Northern Hemisphere annular mode. Consequently, it was proposed that the 1993 cyclonic shift in ocean circulation was driven by the shift to the strongly positive AO (Morison et al. 2000).

After the mid-1990s, the AO declined to nearly pre-1989 average conditions by the early 2000s. By 2003 the salinity and temperature structure in the central Arctic Ocean had also nearly returned to the 1950–89 climatology (Morison et al. 2006). However, in 2007 the wintertime AO increased dramatically, and seemingly as a result the density structure and circulation pattern underwent a change similar to that seen in the early 1990s. The Beaufort Gyre intensified and increased in freshwater content (Giles et al. 2012; McPhee et al. 2009; Proshutinsky et al. 2009). However, comparisons by Morison et al. (2012) among dynamic ocean topography (DOT = sea surface height above the geoid) from *Ice, Cloud and Land Elevation Satellite* (*ICESat*) altimetry, ocean bottom pressure (OBP) from the Gravity Recovery and Climate Experiment (GRACE), and repeat hydrographic station data of the North Pole Environmental Observatory (NPEO), Beaufort Gyre Exploration Project (BGEP), and the Nansen–Amundsen Observing System (NABOS) reveal that increased anticyclonic upper-ocean circulation and freshwater content in the Beaufort Sea were almost completely offset by strengthened cyclonic circulation and increased salinity on the Russian side

of the Arctic Ocean. The resulting remote sensing derived trend in deep basin (depth > 500 m) freshwater content was consistent with the total of offsetting Canada and Eurasian Basin hydrography derived trends over the previous decade (Rabe et al. 2011).

Other satellite altimetry studies also report increased cyclonic Arctic Ocean surface circulation with increased AO (Armitage et al. 2018). *Environmental Satellite* (*Envisat*) DOT from 2003 to 2011 and *CryoSat-2* DOT from 2011 to 2014 show increases in DOT on the Russian margins of the Arctic Ocean and corresponding west to east circulation under positive phases of the AO. Although *Envisat* gives monthly temporal resolution, the latitude limitations of *Envisat* do not allow observation of the central Arctic Ocean and possible dipole character of the cyclonic mode.

The dipole character of the changes in upper-ocean surface circulation in 1993 and again in 2007, namely, more intense anticyclonic circulation in the Beaufort Sea and more intense and pervasive cyclonic circulation in the rest of the Arctic Ocean, is consistent with the shift from anticyclonic to cyclonic regimes of surface circulation of the Arctic Ocean originated by Gudkovich and described in a review by Sokolov (Gudkovich 1961; Morison et al. 2012; Proshutinsky and Johnson 1997; Sokolov 1962). In Sokolov's anticyclonic mode, Arctic Ocean surface circulation is dominated by a large Beaufort Gyre spreading over most of the Arctic Basin. In the cyclonic mode, the Beaufort Gyre is contracted and weakened, and cyclonic surface circulation dominates the Russian side (east longitudes) of the Arctic Ocean extending even to the East Siberian and Chukchi Seas. The main flow of the Transpolar Drift weakens and in the central Arctic Ocean shifts counterclockwise toward North America. Changes in the early 1990s suggest a shift to the cyclonic mode with a smaller, though more intense Beaufort Gyre, a counterclockwise shift in Transpolar Drift axis, and cyclonic surface circulation in the Makarov Basin on Russian side of the Arctic Ocean.

In spite of evidence of the dipole character of the cyclonic mode, and perhaps due to the preponderance of in situ measurements in the Beaufort Sea, the idea persists that the Arctic Ocean upper-ocean circulation is a monopole that is in a more anticyclonic state than in the past (Hofmann et al. 2015; Proshutinsky et al. 2015).

In this paper, we use dynamic heights (1950–89) from the EWG atlas (Timokhov and Tanis 1997a) and dynamic ocean topography from *ICESat* (2004–09) and *CryoSat-2* (2011–19) to demonstrate the cyclonic shift in the upper Arctic Ocean and to show the spatial patterns of the anticyclonic and cyclonic modes of surface circulation. We relate the cyclonic shift and these patterns to changes in the AO.

For the purposes of this paper and consistent with many other studies (e.g., Aagaard and Greisman 1975; Dickson et al. 2000; Timmermans and Marshall 2020), we define as the Arctic Ocean only waters in the Arctic Basin, specifically that region bounded by Fram Strait, the Barents Sea continental shelf break, the Russian coast, Bering Strait, the Canadian Archipelago and northern Greenland. The development of the modes of variability is further constrained to the deep Arctic Basin because our record of dynamic heights prior to 1989 is the Environmental Working Group's Joint U.S.–Russian Atlas of the Arctic Ocean for the Winter Period (Gore and Belt 1997; Timokhov and Tanis 1997a), and the analysis area of this atlas is limited to the so-called ''Gore Box'' in the deep ocean. We will be referring to deep subbasins such as the Eurasian Basin including the Nansen and Amundsen basins on the Russian–European side of the Lomonosov Ridge, which lies across the North Pole roughly along 45°W–135°E (Fig. 1a). The Eurasian Basin is fed from the Nordic seas (Norwegian and Greenland Seas) through the deep Fram Strait and across the shallow Barents Sea shelf. On the Canada–U.S. side of the Lomonosov Ridge we will often refer to the Makarov Basin, that V-shaped basin between the Lomonosov Ridge and the Alpha–Mendeleyev ridge system aligned with 180° longitude (Fig. 1a). The Canada Basin refers to the remainder of the area on the Canada–U.S. side of the Alpha–Mendeleyev ridges and is fed by the shallow Bering Strait from the North Pacific Ocean. We will also describe the primary region of DH and DOT variability as lying on the Russian side of the Arctic Ocean or in east longitudes, and by this we will, where applicable, also be including the shallow Kara, Laptev, and East Siberian shelf seas.

2. Dynamic height, dynamic ocean topography, and AO data

The relative strength of anticyclonic and cyclonic modes of Arctic Ocean upper-ocean circulation is illustrated by a combination of the 1950–89 dynamic height data from the EWG Joint U.S.–Russian Atlas of the Arctic Ocean, Oceanography Atlas for the Winter Period (Timokhov and Tanis 1997a), commonly referred to hereafter as EWG data, and 2003–19 dynamic ocean topography (DOT = sea surface height − Earth Gravitational Model 2008 geoid) from *ICESat* (Kwok and Morison 2011) and *CryoSat-2* (Kwok and Morison 2016; Morison et al. 2018a), commonly referred to hereafter collectively as the satellite DOT data.

The EWG dynamic height data are available at a number of locations including NASA Earthdata at NSIDC (https://cmr.earthdata.nasa.gov/search/concepts/C1386246245-NSIDCV0.html) and by FTP (ftp://sidads.colorado.edu/pub/DATASETS/NOAA/G01961). The atlases were produced under the auspices of the 1993 Gore–Chernomyrdin Agreement to release formerly classified or sensitive data. They were developed by colleagues led by Leo Timokhov at the Arctic and Antarctic Research Institute, using over one million hydrographic stations. They have been used previously in a study of steric heights across the northern seas (Steele and Ermold 2007). The atlases include no original hydrographic profiles. They do include decadal (1950s–1980s) average fields of temperature, salinity, and density versus depth, gridded using objective techniques throughout the so-called Gore Box region (where data could be declassified and corresponding to the area showing data in Figs. 2–6, 10, and 13). Particularly important to this study, the winter atlas also includes, with very few gaps, annual maps from 1950 to 1989 of dynamic heights (DH) at the sea surface computed relative to 200 m from the hydrographic profiles by the dynamic method (Neumann and Pierson 1966),

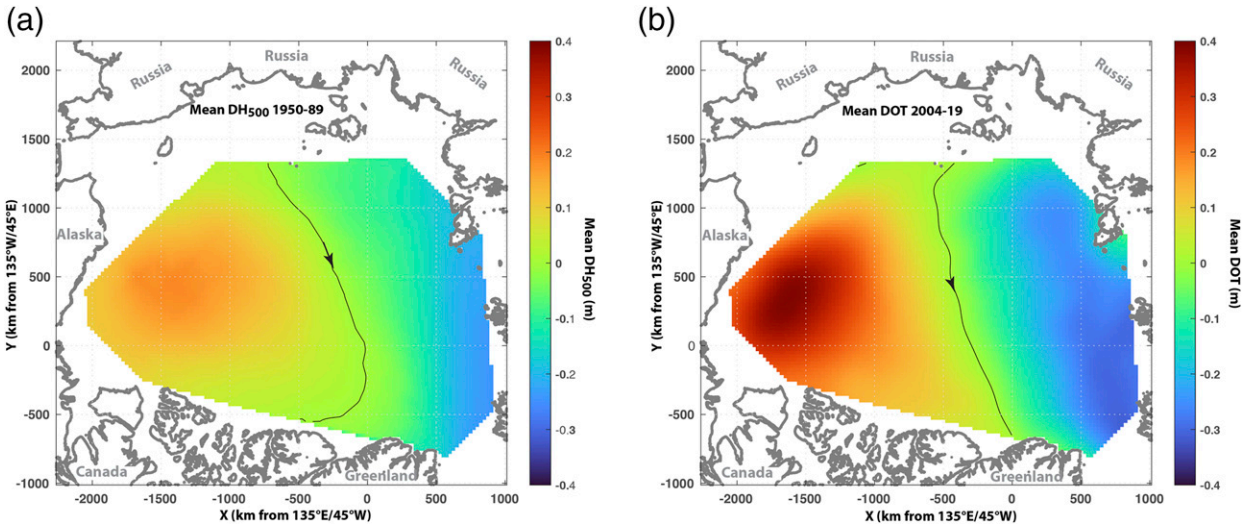

FIG. 2. (a) Time average of anomalies of DH_{500} ($1.113 \times DH_{200}$) about their spatial means from 1950 to 1989 from U.S.–Russian hydrographic measurements. (b) Time average of anomalies of dynamic ocean topography about their spatial means from 2004 to 2019 from *ICESat* and *CryoSat-2* altimetry. Black arrow is on the zero contour.

essentially as the vertical integral of the anomaly of specific volume. While the data include those from ice camps and cruises, much of the winter data coverage is from the wide-ranging Russian Sever (North) aircraft surveys conducted annually in late winter and early spring when conditions were optimum for Arctic sea ice flight operations. Horizontal gradients in these dynamic heights yield surface geostrophic current relative to a 200-m level of no motion. Consequently, maps of DH define surface circulation with geostrophic current anticyclonic around a dome in DH (e.g., the Beaufort Gyre) and cyclonic around a depression in DH.

Dynamic ocean topography is the sea surface height deviation above the geoid. As such, the gradients in DOT drive absolute geostrophic current at the surface. This is in the same sense that gradients in DH drive the surface geostrophic currents relative to the assumed level of no motion. Our satellite DOT data come from the *ICESat* laser altimeter from 2004 to 2009 and the *CryoSat-2* radar altimeter from 2011 to 2019. The *ICESat* DOT in the Arctic Ocean, including the Gore Box, are essentially the same as that described in Kwok and Morison (2011) derived from *ICESat* altimetry from GLA15 version 34 from the NASA Distributed Active Archive Center at the National Snow and Ice Data Center (https://nsidc.org/data/icesat/data.html). The *ICESat* campaigns used here were conducted primarily in February and March of each year.

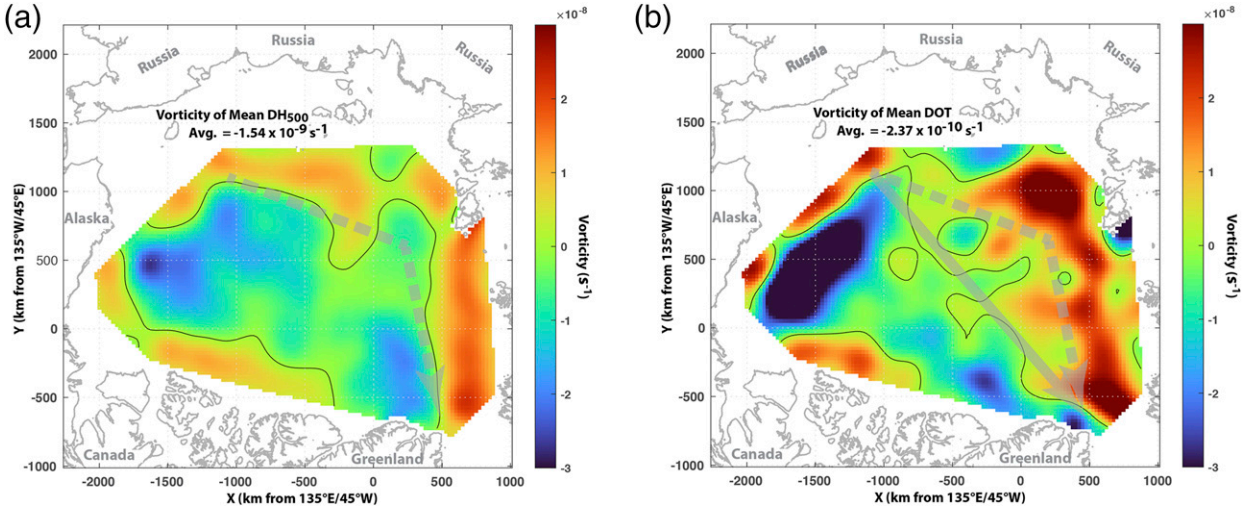

FIG. 3. Average vorticity pattern from (a) the pre-1989 DH_{500} ($1.113 \times DH_{200}$) and (b) from 2004 to 2019, satellite DOT. Gray arrow is notional alignment of the Transpolar Front and Drift corresponding to the zero vorticity contour; dashed line is pre-1990 and solid line is 2004–19.

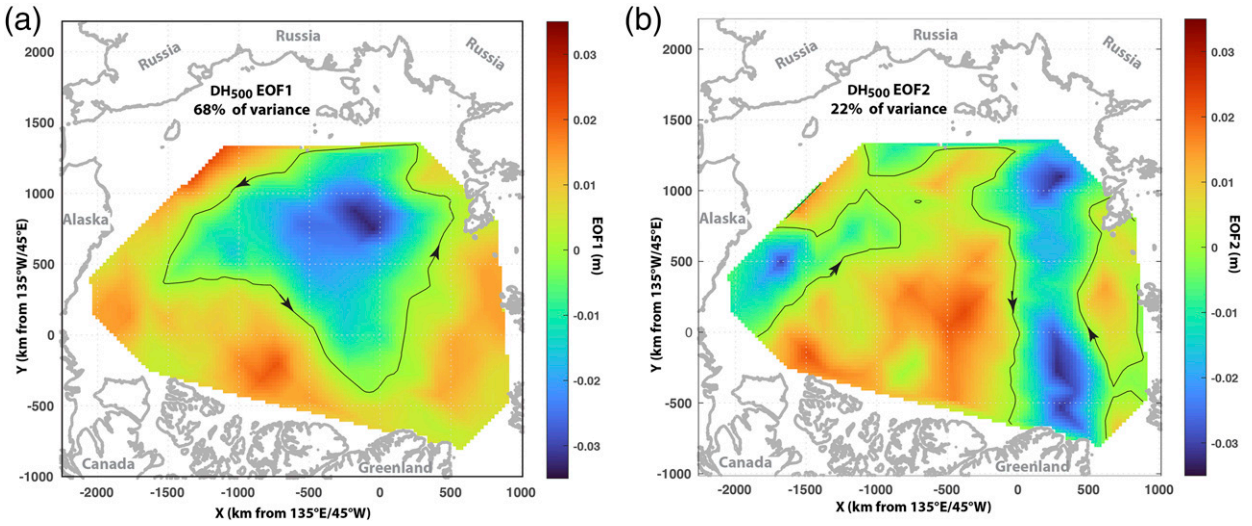

FIG. 4. (a) The first and (b) second EOFs of dynamic height relative to 500 dbar from 1950 to 1989 from U.S.–Russian hydrographic measurements. Arrows indicate geostrophic surface current directions.

CryoSat-2 DOT in the Arctic Ocean is that described Kwok and Morison (2016) but updated to 2019. February and March *CryoSat-2* data are used to better match the late winter, early spring season of the *ICESat* DOT data and the largely late winter to early spring, Sever-derived, pre-1990 DH data. The data are from the Synthetic Aperture Radar (SAR) Interferometric Radar Altimeter (SIRAL) instrument on *CryoSat-2* available through ESA's data portal (https://earth.esa.int). Per Morison et al. (2018a), the DOT data are collected in 25-km grid cells, kriged to fill missing cells, and smoothed with a 200-km Gaussian filter to avoid unresolved geoid errors (McAdoo et al. 2013).

For two examples of transitions in surface circulation under changing atmospheric forcing (Figs. 11 and 12) we use DOT extending into the Nordic seas. The combination of DOT data over the open ocean with those over the ice-covered Arctic Ocean is described in Morison et al. (2018a) and includes the sea state bias correction derived there for *ICESat*. For 2004–09, the Nordic seas *ICESat* data also come from GLA15 version 34 from the NASA Distributed Active Archive Center at the National Snow and Ice Data Center (https://nsidc.org/data/icesat/data.html). For 2011–17 the Nordic seas *CryoSat-2* data come from the Radar Altimeter Database System (RADS, http://rads.tudelft.nl/rads/rads.shtml).

Valid comparisons of historical circulation quantified by hydrography-derived DH with satellite era circulation quantified by altimetry-derived DOT depend on the successful comparison of the patterns of spatial variability of contemporaneous DH and DOT. This has been done using contemporaneous hydrographic measurements of DH with DOT from *ICESat*

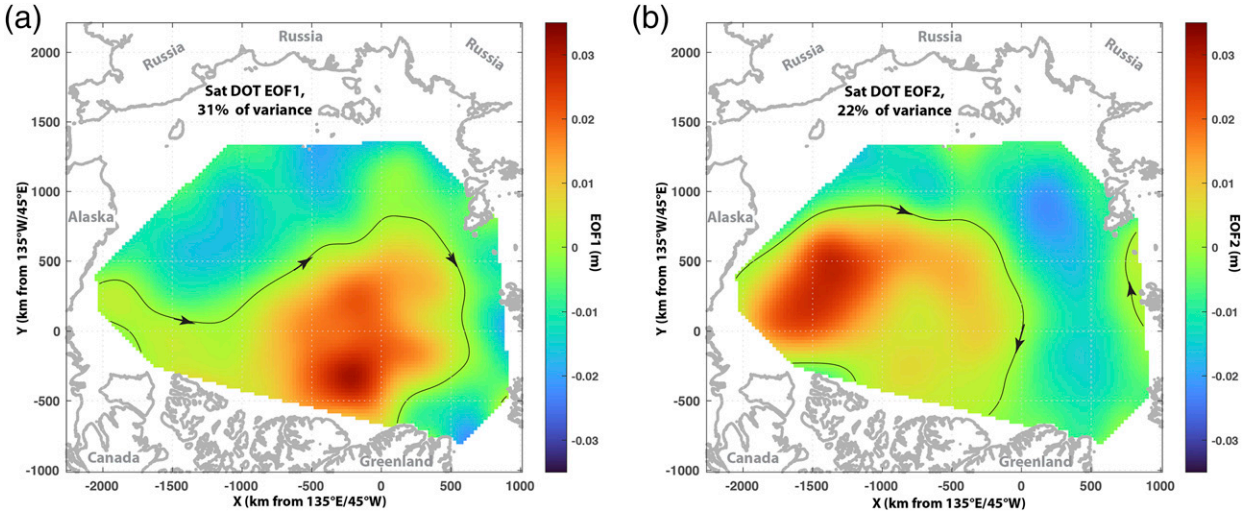

FIG. 5. (a) The first and (b) second EOFs of yearly springtime *ICESat* and *CryoSat-2* 2004–19 DOT spatial variations about the area means. Arrows indicate surface geostrophic current directions.

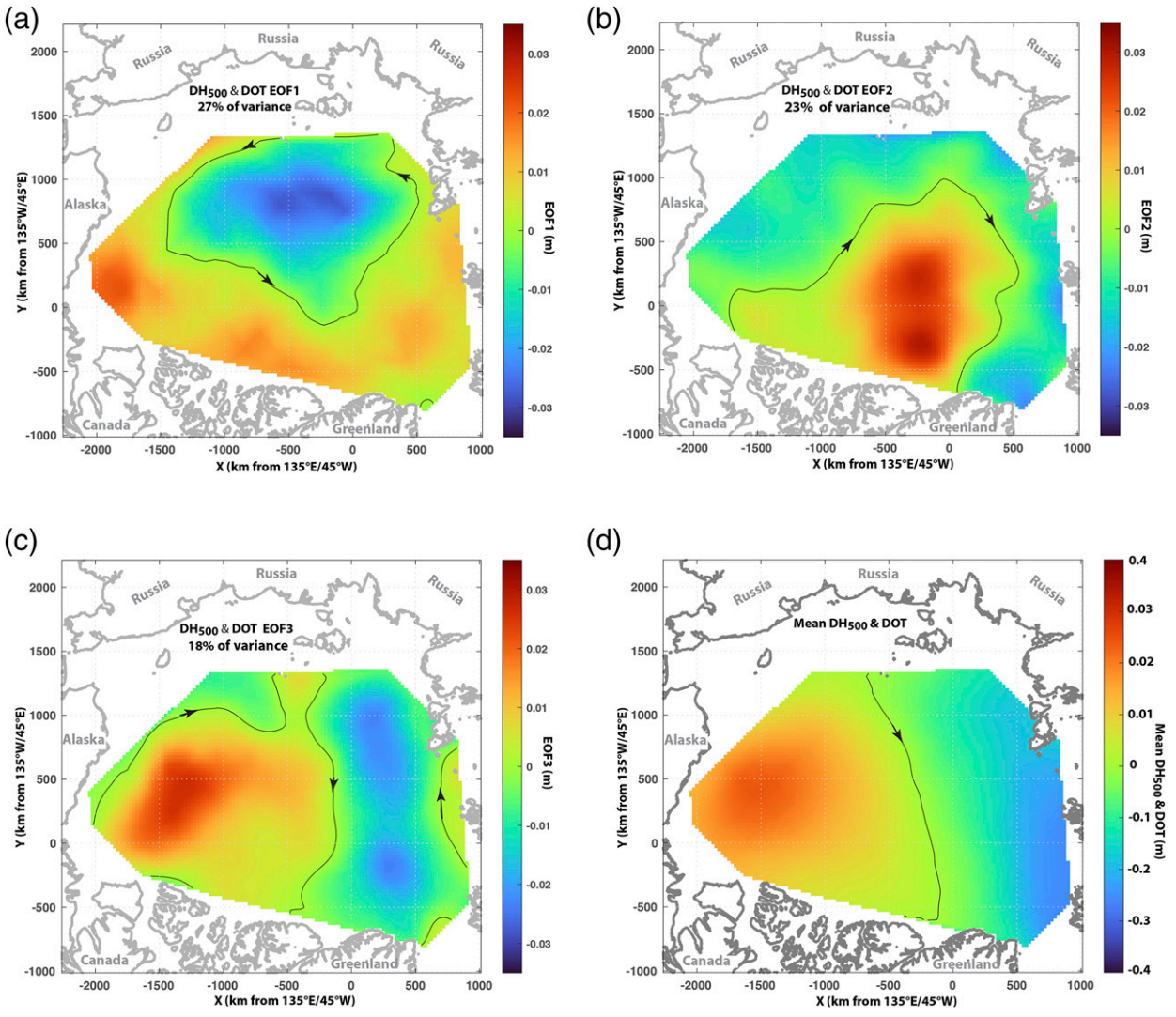

FIG. 6. EOFs of annual anomalies of concatenated DH_{500} and DOT records 1950-2019. (a) First EOF, (b) second EOF, (c) third EOF, and (d) the mean of the concatenated DH_{500} and DOT. Arrows indicate geostrophic surface current directions.

and CryoSat2. Kwok and Morison (2011) compare DOT from *ICESat* with DH relative to a 500-m level of no motion (DH_{500}) from hydrographic stations done in the Canada, Makarov, and Amundsen basins by the North Pole Environmental Observatory (NPEO) and other programs as part of the International Polar Year in 2008. They find excellent correlation, $r = 0.92$ (0.88 to 0.95 for 99% confidence limits). The standard deviation of the difference between DOT and the DH_{500} over all the stations is 7.4 cm over a range of DOT equal to 80 cm.

For a similar comparison of DOT from *CryoSat-2* with DH_{500} from hydrographic stations by the NPEO and Switchyard projects from 2011 to 2014, Kwok and Morison (2016) find a correlation of $r = 0.92$ (0.88–0.95 for 99% confidence limits). The standard deviation of the difference between DOT and the DH_{500} is 3.6 cm over a DOT range of ~30 cm. This result is for stations spanning over 1000 km of ocean including three regions (Makarov Basin, Lincoln Sea, and Amundsen Basin) with markedly different water mass structures.

Thus, we have good agreement between circulation patterns dictated by the spatial variation in satellite DOT and DH_{500} measured in situ. Similar agreement should apply, to comparisons of satellite DOT with DH relative to a 200-m level of no motion (hereafter expressed DH_{200}), with an adjustment discussed below.

Steele and Ermold (2007) needed to infer dynamic heights relative to 1000 m from EWG dynamic heights relative to 200 m. Similarly, we address the difference in circulation patterns indicated by DH_{200} and DH_{500}, by calculating both for the EWG decadal averages of temperature and salinity and comparing the averages of these to each other and to the decadal averages of the EWG annual averages of DH_{200}. The all-time average of the EWG yearly DH_{200} spatial pattern is virtually the same as the all-time average DH_{200} pattern derived from the

EWG decadal temperature and salinity averages. We have also compared DH_{200} and DH_{500} calculated from the EWG decadal averages of temperature and salinity and find very similar spatial patterns with a spatial mean difference of 5.89 cm and standard deviation in the difference of 2.28 cm. The spatial mean difference is irrelevant to spatial gradients and the surface circulation they cause, so only the slight amplification in spatial variability of DH_{500} versus DH_{200} is of concern. We take this as the ratio equal to 1.113 of the standard deviation of the all decade-averaged DH_{500} pattern to the standard deviation of the all decade-averaged DH_{200} pattern. Thus, the gradients and induced circulation associated with annual average DH_{500} may be 11.3% greater in magnitude than gradients and circulation associated with the EWG annual averages of DH_{200}. As we will show, surface circulation patterns in the modern satellite era appear to be more intense than in the past. To ensure that this difference is not exaggerated by comparing DOT to DH_{200}, in what follows we compare DOT to DH_{500} defined as the EWG yearly DH_{200} multiplied 1.113.

Biases between *ICESat* and *CryoSat-2* DOT in the Arctic Ocean and Nordic seas have been addressed previously (Morison et al. 2018a). Because *ICESat* (2004–09) and *CryoSat-2* (from 2010 to present) were never contemporaneous, they were compared through the intermediary of ocean bottom pressure (OBP) from GRACE plus dynamic heights from hundreds of hydrographic profiles from CTD stations, automated drifting buoys, and Argo floats. Specifically, Morison et al. (2018a) find that *ICESat* and *CryoSat-2* DOT from everywhere in the Arctic Ocean, when plotted against DH_{500} plus OBP at hydrographic stations, all fall along a gently curved line defining the relation between DOT and DH_{500} plus OBP. With the inclusion of a 10-cm bias correction to RADS-derived *CryoSat-2* open ocean DOT to match our Arctic Ocean *CryoSat-2* DOT in overlapping regions, and with application of the sea state bias correction for open ocean *ICESat* DOT derived in Morison et al. (2018a), the relation between the satellite DOT and DH_{500} plus OBP extends to the whole of the Arctic Ocean and Greenland and Norwegian seas with a standard deviation of 5.2 cm over a DOT range of 90 cm. Any changes in DOT patterns between the *ICESat-2* DOT and *CryoSat-2* DOT are consistent with hydrographic plus OBP changes.

Monthly averages of the AO index are taken in tabular form from NOAA/NCEP (https://www.cpc.ncep.noaa.gov/products/precip/CWlink/daily_ao_index/monthly.ao.index.b50.current.ascii.table). For winter averages each year, YYYY, we average YYYY 1 November and December and YYYY January–April to form the winter average for year YYYY. Additionally, to look at the correlations between the AO and the ocean principal component time series, we use 12-month moving averages computed at each month.

3. Mean fields of dynamic height 1950–89 and DOT 2004–19

Comparison of the 1950–89 DH_{500} ($1.113 \times DH_{200}$) average spatial variability pattern (Fig. 2a) with the 2004–19 satellite DOT average spatial variability pattern (Fig. 2b) reveal fundamental spatial changes. The mean of 1950–89 yearly DH_{500} is dominated by the Beaufort Gyre, which in this case occupies more than half the area of the Gore Box. The average pattern of the combined DOT from *ICESat* (2004–09) and *CryoSat-2* (2011–19) (Fig. 2b) is similar, but the Beaufort Gyre is more intense but smaller in area, and the area of low DOT in the Eurasian Basin is larger and deeper. The result is that in the satellite period the increased intensity of the Beaufort Gyre is offset by increasingly cyclonic surface circulation over an ever-greater share of the rest of the Arctic Ocean. The impact of this on circulation is revealed by comparison of the vorticity associated with the average of 1950–89 annual winter dynamic heights (Fig. 3a) and vorticity from the average DOT from *ICESat* 2004–09 and *CryoSat-2* 2011–19 (Fig. 3b).

Vorticity is the curl of velocity and because velocity acts to the right of the gradient in DOT or DH, vorticity is proportional to the Laplacian of DOT. In Fig. 3, vorticity Ψ is calculated as $\Psi = (g/f)\nabla^2 h$, where h is DH_{500} or DOT. Under cyclonic (anticyclonic) circulation vorticity is positive (negative). Comparison of the 1950–89 mean of Arctic Ocean vorticity (Fig. 3a) and vorticity of the 2004–19 yearly DOT (Fig. 3b) show that in the recent decades, the Beaufort Gyre intensified but contracted in size while the cyclonic circulation in the Eurasian Basin intensified and spread. The axis of the Transpolar Drift, taken as the zero-vorticity contour, is shifted on average approximately 30° counterclockwise, characteristic of the cyclonic shift of surface circulation change in the early 1990s (Fig. 1b). The change in vorticity patterns has resulted in an increase of area-average Arctic Ocean vorticity from -15 to $-2.37 \times 10^{-10}\,s^{-1}$. The satellite era Arctic Ocean surface circulation is almost a factor of 7 less anticyclonic than the pre-1990 Arctic Ocean circulation. As a whole Arctic Ocean surface circulation now is more cyclonic than it was prior to 1990.

We have also compared the 1950–89 and 2004–19 vorticity patterns normalized by their individual standard deviations and find that associated with the cyclonic rotation in the axis of the Transpolar Drift about an anchor point in Fram Strait, the cyclonic surface circulation in the Eurasian Basin has spread at the expense of the size of the Beaufort Gyre so that the fraction of area of positive (cyclonic) vorticity has increased from 42% to 55%. In terms of area, the surface of the deep Arctic Ocean has gone from being anticyclonic to cyclonic. Essentially, the anticyclonic vorticity of the Beaufort Gyre and its dominance prior to 1990 has been more than offset by increasingly cyclonic surface circulation in the rest of the Arctic Ocean and a decrease in the area of the Beaufort Gyre.

4. Modes of Arctic Ocean surface circulation variation

Dominant modes of variability of the Arctic Ocean are objectively characterized by EOF analysis of the pre-1989 dynamic heights (Fig. 4) and the satellite era dynamic ocean topography (Fig. 5). The EOF analysis for pre-1989 surface circulation variability is done on the anomalies of 1950–89 yearly EWG DH_{500} spatial patterns about the mean spatial pattern of DH_{500} (Fig. 2a). The first EOF DH_{500} (Fig. 4a) explaining 68% of the variance features a major depression centered in the Makarov Basin and a

smaller intense dome near the Canadian Archipelago plus less raised areas around the rest of the basin margins. In positive phase it epitomizes cyclonic mode as revealed by the *Pargo* 1993 salinity anomaly (Fig. 1b) in the Makarov Basin (Fig. 1a). The second EOF (Fig. 4b) explaining 22% of the variance is a dipole variation between the northern Canada and Eurasian basins. Neither EOF resembles the Beaufort Gyre as exemplified by the average dynamic height (Fig. 2a).

The EOFs of yearly springtime, *ICESat* and *CryoSat-2* 2004–19 DOT anomalies (Fig. 5) about the mean spatial pattern (Fig. 2b) are similar to the EOFs of the yearly winter EWG dynamic height anomalies (Fig. 4). The first EOF of the 2004–19 DOT (Fig. 5a) explains 31% of the variance. It is similar to EOF1 of 1950–89 DH_{500} (Fig. 4a) in showing a depression on the Russian side of the Arctic Ocean and a high near the Canadian Archipelago, but the depression has a broader extent along the Russian continental shelf break consistent with the Sokolov cyclonic mode and as seen in the DOT transitions under increasing AO in 2007 (Morison et al. 2012). Also, relative to the 1950–89 EOF1, the high in the 2004–19 EOF1 is shifted east and is expanded, extending between Ellesmere Island–Greenland and the North Pole. If we characterize the first EOFs as dipoles, the satellite era dipole is rotated counterclockwise about 25° from the 1950–89 dipole. The second EOF of the 2004–19 DOT (Fig. 5b) explains 22% of the variance and is similar to EOF2 of the EWG DH_{500} anomaly record (Fig. 4b) except that the western Arctic high extends into the Beaufort Sea.

The temporal mean of concatenated EWG DH_{500} and satellite DOT patterns (Fig. 6d) looks like an intensified version of the DH_{500} mean pattern, likely because the DH_{500} record is 3 times longer than the DOT record.

The first EOF of the concatenated DH_{500} and DOT anomaly record (Fig. 6a) is similar to the EOF1 of the EWG DH_{500} record (Fig. 4a) and explains 27% of the combined DH_{500} and DOT anomaly record variance. The second EOF of the concatenated DH_{500}–DOT anomaly record (Fig. 6b) is similar to the EOF1 of the DOT record (Fig. 4a) and explains 23% of the DOT record variance. In terms of explained variance, the first two EOFs are not statistically well separated (North et al. 1982), but together they represent the combined first EOFs of the individual DH_{500} and DOT anomalies. The first EOF emphasizes the strong depression in the Makarov Basin characteristic of EOF1 of the DH_{500} anomaly. The second EOF represents in addition, the longer arced depression spread across the Russian side of the deep Arctic Ocean and the Greenland–North Pole bull's-eye, both characteristic of EOF1 of the 2004–19 DOT anomaly.

The third EOF of the concatenated DH_{500}–DOT anomaly (Fig. 6c) explains 18% of the variance and corresponds closely to the Eurasian Basin versus Canada Basin dipole of the second EOFs of the individual DH_{500} and DOT records.

The principal component (PC) time series (Fig. 7) for the first (in green) and second EOFs (in blue) of the concatenated DH_{500}–DOT anomalies are in phase with PC1 dominant prior to 1989. In the satellite period PC1 and PC2 show initial highs followed by substantial lows, with PC2 showing larger swings but appearing to lag behind PC1. This is likely a reflection of representing two aspects of the same mode of variability corresponding to the first EOFs of the individual DH_{500} (Fig. 4a) and DOT (Fig. 5a). After 2012 and a major drop in both PC1 and PC2, PC1 rises followed by PC2, suggesting cyclonic surface circulation on the Russian side of the Arctic Ocean followed by drops at the end of the record.

5. Examples of the cyclonic mode

Sokolov's review (Sokolov 1962) following Gudkovich (Gudkovich 1961) indicates the cyclonic mode prevails when the Icelandic low is strong relative to the Beaufort high, and it describes the Icelandic low as "influencing a vast territory of the ocean from Iceland to the New Siberian Islands" and argues that "wind conditions caused by it induce a cyclonic-type circulation of surface waters in the Greenland, Norwegian, Barents, Kara, and Laptev seas." The time-average sea level atmospheric pressure (SLP) over the marine Arctic is dominated by the Beaufort high over the Arctic Basin and the Icelandic low over the Nordic and Barents Seas (Fig. 8a). However, the strengthened Icelandic low pressure pattern Sokolov describes is essentially the sea level pressure pattern of the Arctic Oscillation shown here as the regression map of the NOAA/NCEP AO principal component time series on SLP from 1950 to 2019 (Fig. 8b). The AO pattern in the Arctic strengthens the Icelandic low and may weaken part of the Beaufort high. In modern terms, the cyclonic mode prevails when the AO is high.

Since reaching a maximum value in 1989, the winter [November–April (NDJFMA)] AO from NOAA/NCEP (Fig. 9) has averaged about one standard deviation above the 1950–88 average. Specifically, from 1950 to 1988 the winter (NDJFMA) AO averaged −0.4288 with a standard deviation of 0.5788. From 1989 to 2019 the winter AO averaged 0.1624 with a standard deviation of 0.7623. Thus, the AO in 1989–2019 is 0.591 18 higher than the winter AO in 1950–88. It appears from Fig. 9 that year-to-year the winter AO values are largely independent, but even if we assume a lack of independence reduces degrees of freedom by half, the increase in AO between the early period and the recent period is 2.55 times the standard error of the means (single-tailed $p = 0.0082$) and is statistically significant at the 99% level. The increase in multiyear average winter AO combined with the cyclonic pattern of the AO regressed on SLP (Fig. 8b) likely explain the increased average vorticity of the Arctic Ocean in the satellite period relative to pre-1989 (Fig. 3).

Notable shifts in the AO in 1989–90, 2007, and 2010 reveal how the Arctic Ocean responds to interannual changes in global scale atmospheric circulation.

The USS *Pargo* results from 1993 reflect the AO maximum in 1989 and values of winter AO through 1995 that were at least one standard deviation above the average prior to 1989. The positive salinity anomaly (Fig. 1b) in 1993 across the Makarov Basin (Fig. 1a) is, by virtue of its effect on reducing dynamic heights, characteristic of the cyclonic mode.

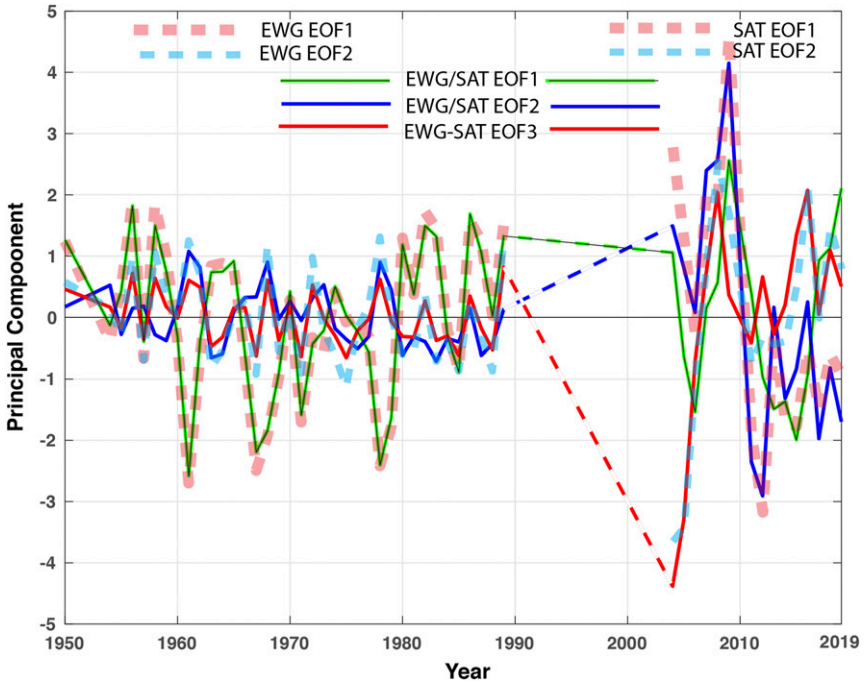

FIG. 7. Principal component time series for the first three EOFs of the concatenated DH_{500} and DOT anomaly records: PC1 in green, PC2 in blue, and PC3 in red. PC1 for separate DH and DOT (pre- and post-1980) are shown as broad red dashed lines, and PC2 for separate DH and DOT are shown as broad blue dashed lines.

We have calculated DH_{500} at the *Pargo* CTD stations and the associated dynamic height anomaly, DH_{Pargo}, pattern relative to the overall mean DH_{500} pattern prior to 1990. A least squares fit to the variation of DH_{Pargo} with a linear combination of the first and second EOFs, A_{e1}EOF1 + A_{e2}EOF2, for the EWG record (Fig. 4) evaluated at the *Pargo* locations results in $A_{e1} = 6.8069$ and $A_{e2} = -0.2953$ and explains 68% of the variance in DH_{Pargo}. The EOF1 component accounts for 97% of this and the DH_{Pargo} variation divided by A_{e1} agrees closely with the EWG EOF1 at the *Pargo* stations (Fig. 10a). The *Pargo* dynamic height pattern after the record high AO is explained overwhelmingly by a strong positive contribution of the first EOF indicative of the cyclonic mode.

Similarly, a least squares fit to the variation of DH_{Pargo} with a linear combination of the first and second EOFs, A_{s1}EOF1 + A_{s2}EOF2, for the satellite DOT record (Fig. 5) evaluated at the *Pargo* locations results in $A_{s1} = 5.5947$ and $A_{s2} = -5.8164$ and explains 63% of the variance in DH_{Pargo}. The EOF1 component accounts for 89% of this and the DH_{Pargo} variation divided by A_{s1} agrees reasonably with the satellite era EOF1 at the *Pargo* stations (Fig. 10b) though not quite as well as it agrees with the EWG era EOF1 (Fig. 10a), which explains about 10% more of the *Pargo* variance.

Finally, in terms of the combined EWG and satellite periods (denoted by h) mean and first three EOFs (Fig. 6), the fit to the *Pargo* anomaly results in $A_{h1} = 4.9648$, $A_{h2} = 1.3078$, and $A_{h3} = 0.0260$ and explains 76% of the variance in DH_{Pargo}. The EOF1 component accounts for nearly 58% of this and the EOF 2 component 42%. The DH_{Pargo} variation divided by A_{h1} agrees with the combined record EOF1 at the *Pargo* stations (Fig. 10c) to a degree similar to the agreement with the pre-1989 EOF1. This is likely because the 1993 *Pargo* cruise was closer in time to the EWG era than the satellite era, and of the combined record EOFs, EOF1 (Figs. 6a and 10b) is most similar to the EWG era EOF1 (Figs. 4a and 10a). No matter whether we compare the *Pargo* dynamic height anomaly pattern to the pre-1989 pattern, the satellite era pattern, or the combined pattern, the anomaly pattern reflects a strong shift to the EOF1 pattern consistent with the cyclonic mode in response to a large and prolonged positive phase of the AO.

Through the 1990s the AO relaxed to near the pre-1989 average by 2003, and hydrographic observations suggest the ocean characteristics near the North Pole had relaxed by 2003 to near pre-1989 conditions as well (Morison et al. 2006).

In 2007, the winter AO increased two standard deviations from pre-1989 average levels and remained high in 2008 and 2009 (Fig. 9). Over this time, *ICESat* DOT trends, as well as changes in DH minus GRACE OBP at repeat hydrographic stations indicate that the Beaufort Gyre intensified (Morison et al. 2012). However, at the same time a DOT trough centered in the Makarov Basin region and aligned with the Russian shelf break deepened and produced more cyclonic circulation on the Russian side of the Arctic Ocean (Morison et al. 2012). Comparison of 2005–06 DOT (Fig. 11a) and 2008–09 DOT (Fig. 11b) illustrates the same trends. The deepening trough illustrated by the difference between 2005–06 and 2008–09 DOT (Fig. 11c) is consistent with EOF1 of pre-1990 dynamic height (Fig. 4a) and EOF1 of satellite-era DOT (Fig. 5a). The

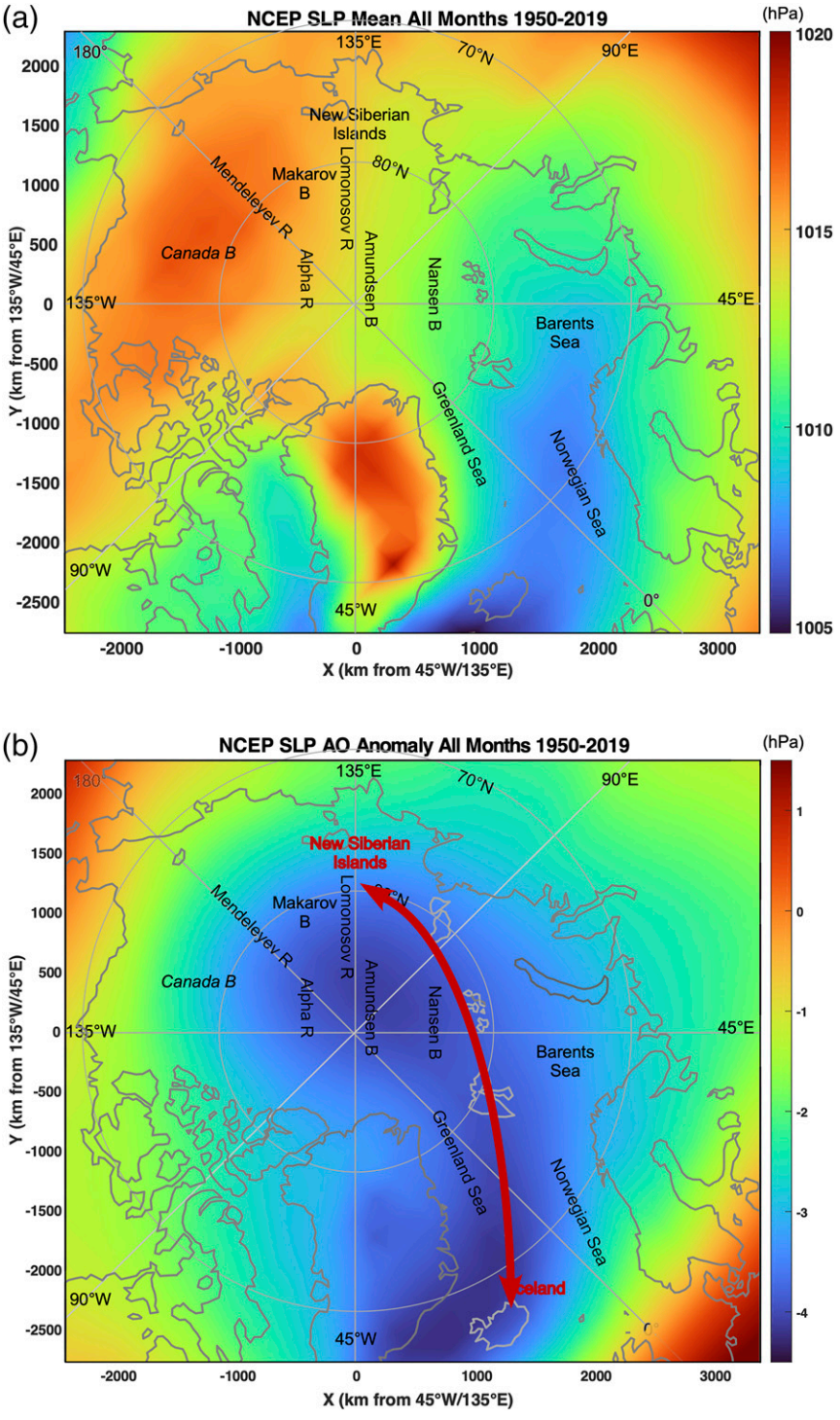

FIG. 8. (a) SLP mean and (b) the SLP anomaly relative to the mean regressed on the NCEP CPC AO from 1950 to 2019 with the notional Icelandic low (red) as described by Sokolov (1962).

extension of the trough east as far as the Chukchi Sea is particularly similar to the satellite era EOF1 (Fig. 5a) and the combined record EOF2 (Fig. 6b). The intensified cyclonic surface circulation included increasing eastward alongshore flow at the Russian coast, which caused increasing amounts of Eurasian runoff to be advected eastward along the Russian coast to ultimately freshen the Beaufort Sea in agreement with freshwater component trends derived from in situ chemical

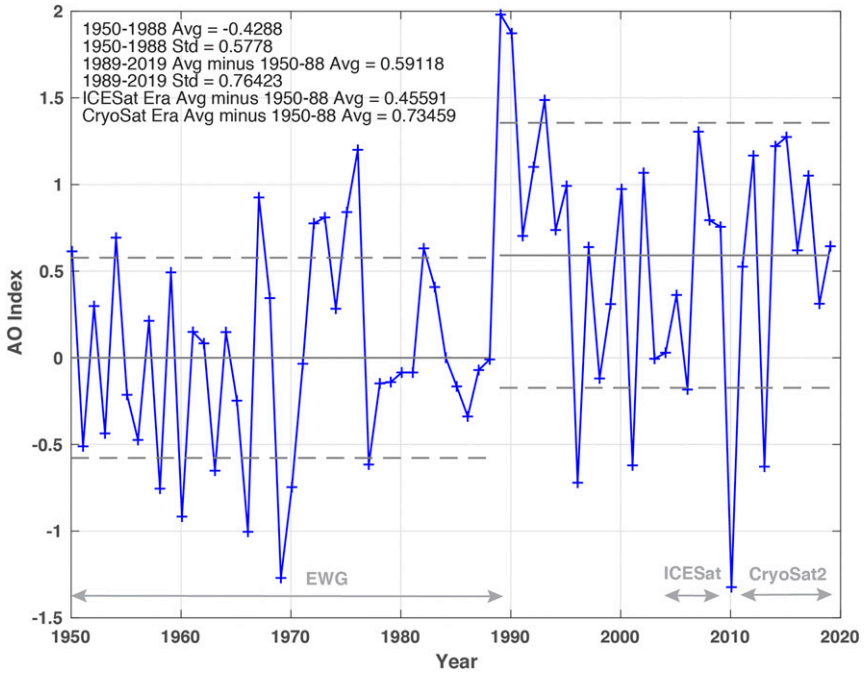

FIG. 9. The winter (NDJFMA) AO index, 1950–2019, minus the average winter AO index from 1950 to 1988.

tracer analysis (Alkire et al. 2015; Morison et al. 2012). Freshwater content estimated from the difference between DOT trends from *ICESat* and OBP trends from GRACE show that the increase in freshwater content of the Beaufort Sea was almost completely balanced by the decrease in freshwater content in the Russian-side trough in a manner suggestive of the early 1990s process weakening the cold halocline (Steele and Boyd 1998).

After 2007, DOT increased in the Barents and Kara Seas in keeping with the increase toward the shore all along the Russian coast (in the Eurasian and Makarov basins and east longitudes of the Canada Basin). The changes in the Nordic seas are somewhat mixed. As in the Eurasian Basin, increased cyclonic surface circulation occurred in the Norwegian Sea (Fig. 11c), but raised DOT along the middle of the Greenland Sea resulted in an anticyclonic shift there and a cyclonic tendency over the northern part of the East Greenland shelf. The cyclonic change in Fram Strait, aided by the anticyclonic change in the Barents Sea, would reinforce the inflow of Atlantic Water in the West Spitsbergen Current and export of Arctic Surface Water along the Northeast Greenland Shelf.

In 2010 the winter AO index reached a record minimum, and the resulting surface circulation changes were the opposite of those we saw in response to the AO increase in 2007. Following the positive transition in 2007–08, the winter AO in 2009 was moderately high, 0.7557, relative to the pre-1989 average. In 2010, the AO reached a record minimum, −1.32, relative to the pre-1989 average (Fig. 9), and in 2011 the AO returned to a positive level, 0.5262 relative to the pre-1989 average. There are no altimeter data for most of 2010, but comparison of the 2008–09 average Arctic Ocean DOT (Fig. 12a) with the 2011–12 average Arctic Ocean DOT (Fig. 12b) illustrates the transition from the cyclonic to anticyclonic mode of surface circulation resulting from the negative impulse of the 2010 AO. The average *ICESat* DOT 2008–09 (Figs. 11b and 12a) shows a strong cyclonic pattern with trough extending eastward into the Russian side of the Canada Basin roughly aligned with the continental shelf break. The average *CryoSat-2* DOT in 2011–12 (Fig. 12b) shows a strong anticyclonic pattern with only a relatively shallow trough in east longitudes of the Canada Basin. Changes in DOT between the 2008–09 *ICESat* DOT and the 2011–12 *CryoSat-2* DOT (2011–12 DOT minus 2008–09 DOT; Fig. 12c) show a DOT increase along Russian side of the Arctic Ocean that is almost the exact opposite of the DOT decrease (Fig. 11c) after the 2007 increase in the AO (Fig. 9).

After 2010, DOT increased in the Barents Sea but remained nearly the same in the Kara Sea resulting in an anticyclonic change on the Barents Shelf in keeping with the Eurasian Basin change. The DOT increase in the Barents Sea also spread west to the Northeast Greenland shelf and the northern Greenland Sea suggesting an anticyclonic surface current tendency that would enhance ice and freshwater export in eastern Fram Strait working against the prevailing inflow of Atlantic Water in the West Spitsbergen Current. Counter to this, increased DOT along the Norwegian coast resulted in northward alongshore flow and a cyclonic tendency in the southern half of the Nordic seas (Fig. 12c).

While the DOT response to the AO increase in 2007 and decrease in 2010 in the east longitudes of the Arctic Basin are simple opposites (decrease after 2007 and increase after 2010), such a simple comparison is not possible for the Barents, Kara, and Nordic seas. This is likely because the Barents Sea has its own response to changes in the NAO (AO) (Smedsrud et al. 2013),

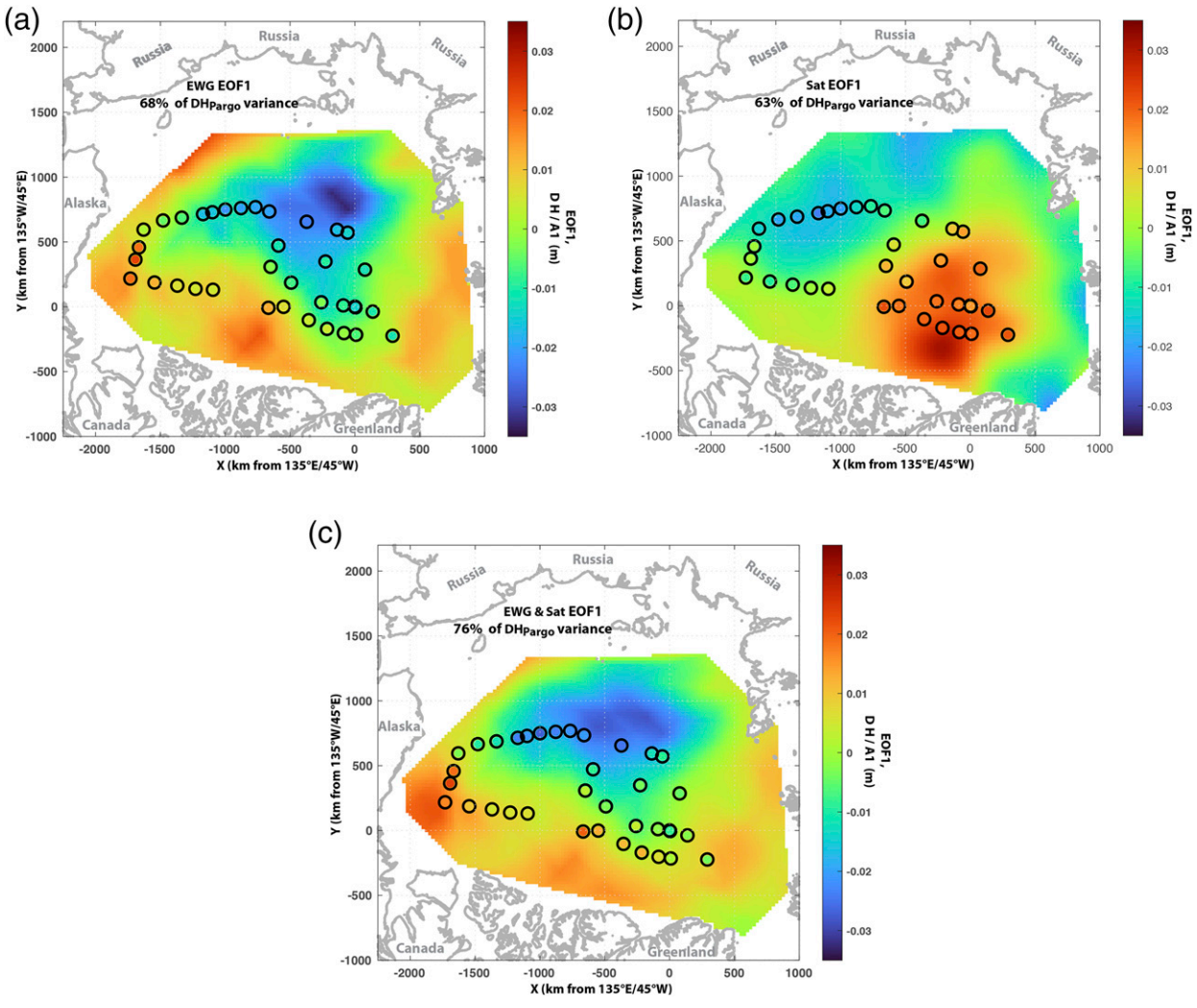

FIG. 10. Anomalies of dynamic height at the *Pargo* stations, DH_{Pargo}, (a) relative to the EWG mean dynamic height (Fig. 2a) overlaid on the EWG-era EOF1 (Fig. 4a) with a common color scale, (b) relative to the satellite mean DOT (Fig. 2b) overlaid on the satellite era EOF1 (Fig. 5a), and (c) relative to the mean of the combined EWG DH_{500} and satellite DOT (Fig. 6d) overlaid on combined record EOF1 (Fig. 6a).

and as we will show, the response of the Barents and Nordic seas to the AO may be more immediate than in the Arctic Basin.

6. The spatial–temporal impact of the Arctic Oscillation on surface circulation

The spatial–temporal impact of the AO on Arctic Ocean surface circulation over the full 1950 to 2019 period is illustrated by projecting the AO principal component time series on the annual DH_{500} and DOT records to find the spatial pattern most highly correlated with the AO. It has been shown that the ocean temperature and salinity anomalies relative to climatology at the North Pole have appeared to follow the AO as a first-order response with a time constant of 5 years and a delay of 3 years (Morison et al. 2006). The rationale for such a characterization is that we expect the response of these upper-ocean temperature and salinity anomalies to be a lagged and smoothed result of atmospheric forcing and to involve transport delays required for the effect of surface and boundary fluxes on temperature and salinity to be transported at depth at the North Pole (e.g., Swift et al. 1997). At the other temporal extreme, we have also seen the strength of the Beaufort Gyre in summer to be correlated with monthly AO at a lag of 2 months (Dewey et al. 2017).

Looking at the interannual changes in upper-ocean circulation at basin scales, the response to the positive AO transition in 2007 (Fig. 11) and the negative transition in 2010 (Fig. 12) suggests the surface circulation responds with a delay of about a year. Consequently, we have projected the annual wintertime (NDJFMA) AO filtered with time constants of 1 year and lags of 0–3 years on the composite DH_{500} and

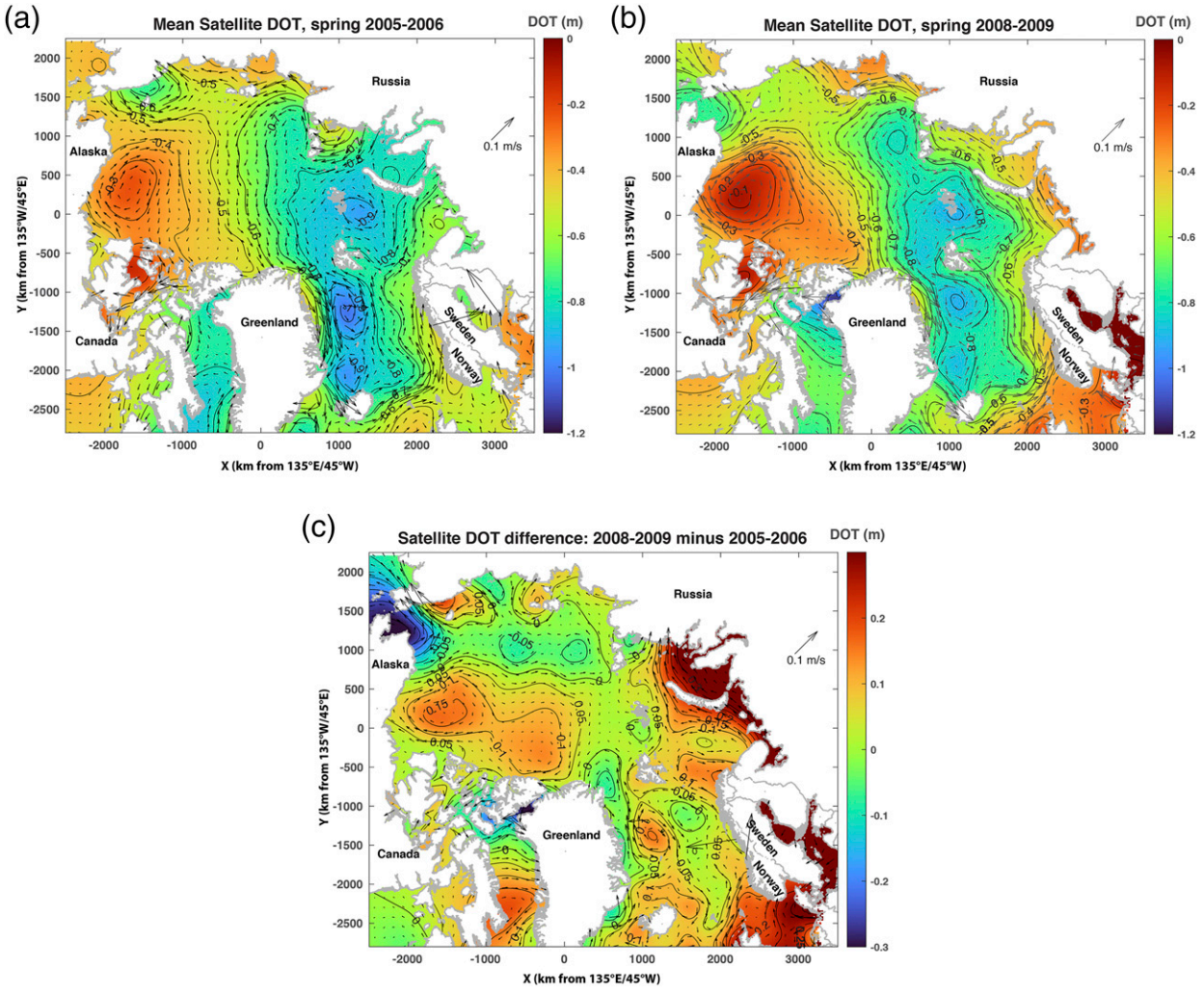

FIG. 11. Average *ICESat* DOT (a) 2005–06 and (b) 2008–09. (c) 2008–09 *ICESat* DOT minus 2005–06 *ICESat* DOT shows a DOT decrease along Russian side of the Arctic Ocean, and an increase on the Canadian side.

satellite DOT records (Fig. 13). We find the projections with an assumed first-order time constant of 1 year show patterns suggestive of an Arctic Ocean response that moves around the Arctic Basin starting in the Eurasian Basin over a 3-yr period.

Recognizing that there is a delay associated with the 1-yr time constant even at zero-lag, the zero-lag projection (Fig. 13a) indicates that DOT depression in the Nansen and Amundsen basins responds relatively quickly to an increase in the AO consistent with atmospheric pressure pattern of the AO in that region (Fig. 8b). However, around the rest of the periphery of the data domain, the projection shows elevated DOT indicating a basin-wide cyclonic pattern similar to other unlagged AO-positive composites of circulation (Armitage et al. 2018; Kwok 2000; Zhang et al. 2003).

The 1-yr lagged projection (Fig. 13b) shifts the DOT depression farther into the Arctic Ocean to the Makarov Basin and also shows a doming in the Canadian Basin. This pattern is consistent with the dominant pattern of change as described by the combined EWG DH_{500} and satellite DOT records (Fig. 6a), the salinity anomaly pattern evidenced by the 1993 *Pargo* data (Figs. 1 and 10c), and the change in DOT one year after the 2007 increase in the AO (Fig. 11c). It is the opposite of the change in DOT one year after the record low in the AO in 2010 (Fig. 12c). Overall, it typifies the dipole character of the cyclonic mode as we have come to know it since 1990 (Morison et al. 2012) with surface depression and cyclonic surface circulation on the Russian side of the basin opposite a rising surface and spinup of anticyclonic surface circulation in the west longitudes of the Canada Basin, the Beaufort Sea, and extending up into the central Arctic Ocean. The 1-yr lagged projection is also similar to the opposite of the change in DOT one year after the 2010 record minimum in the AO (Fig. 12c). This is with the exceptions that for 2010 (Fig. 12c), the response on the Canadian side is more heavily concentrated in the central Arctic Ocean, and the response in the Nansen and Amundsen Basins is stronger than in the projection (Fig. 13b).

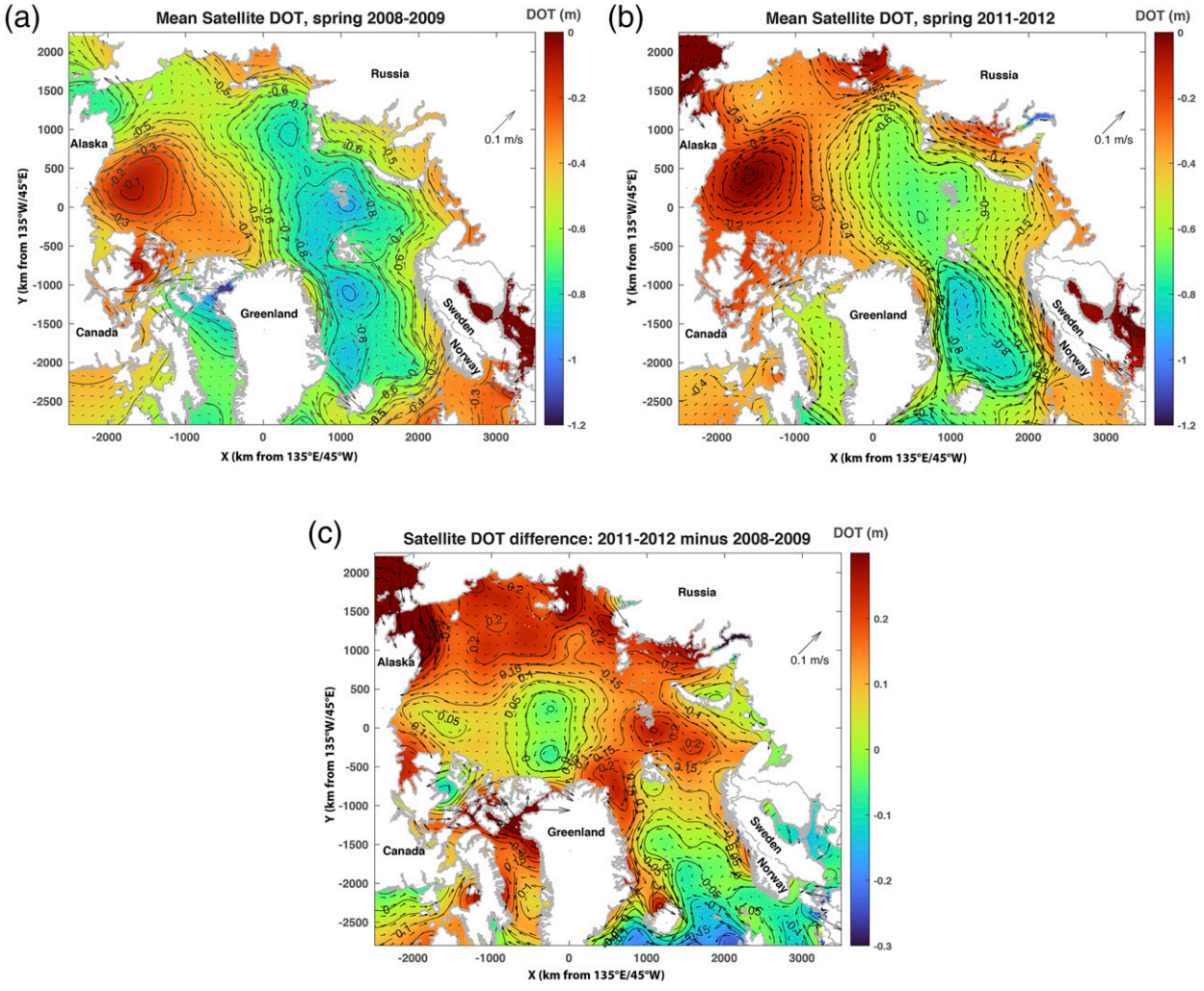

FIG. 12. (a) Average *ICESat* DOT 2008–09 and (b) *CryoSat-2* DOT 2011–12. (c) Average *CryoSat-2* DOT 2011–12 minus *ICESat* DOT 2008–09 shows a DOT increase along Russian side of the Arctic Ocean, and a slight decrease on the Canadian side.

Figure 12c suggests that the absence of a more definitive anticyclonic change in the Nordic seas may be related to the more immediate response of DOT to the AO in the Eurasian Basin near Fram Strait (Fig. 11a) and Nordic seas. The apparent counterclockwise progression of the ocean's response to the AO (Fig. 13b vs Fig. 13a) suggests that in 2011, while the negative AO of 2010 lagged 1 year was forcing a DOT increase in the Makarov Basin (Fig. 11b), the unlagged positive AO of 2011 may have been forcing depression of DOT in the Nordic seas.

The AO response appears to begin to relax after two years. The 2-yr lagged projection (Fig. 13c) shows persistent though less significant surface depression in the Makarov Basin, decreased doming shifted eastward in the Beaufort Sea, and a rebound of DOT near the Fram Strait entrance to the Arctic Ocean.

After three years the ocean seems to rebound from the AO response. The 3-yr lagged projection (Fig. 13d) is significantly positive around the Russian margins of the Arctic Ocean and significantly negative in the central Arctic Ocean. It is also positive in the Beaufort Sea.

7. The temporal relation between the AO and the cyclonic mode of surface circulation

The temporal impact of the AO on Arctic Ocean surface circulation over the full 1950–2019 period is illustrated by comparing the principal component time series of EOF 1, PC1, with the first-order response (1-yr time constant) of the running annual average AO lagged 1 year (Fig. 14). This is the temporal counterpart of Fig. 13b. To better resolve the time differences between the surface height observations (centering on March for DH_{500} and DOT and September for the *Pargo* $DH_{500,}$) we use moving 12-month moving averages of monthly AO rather than NDJFMA winter averages of AO. The 12-month averages AO (gray line in Fig. 14) look virtually the same as the winter averages of AO (Fig. 9) except the minima in 1961 and 1969 are lower in the 12-month averages, and the 12-month

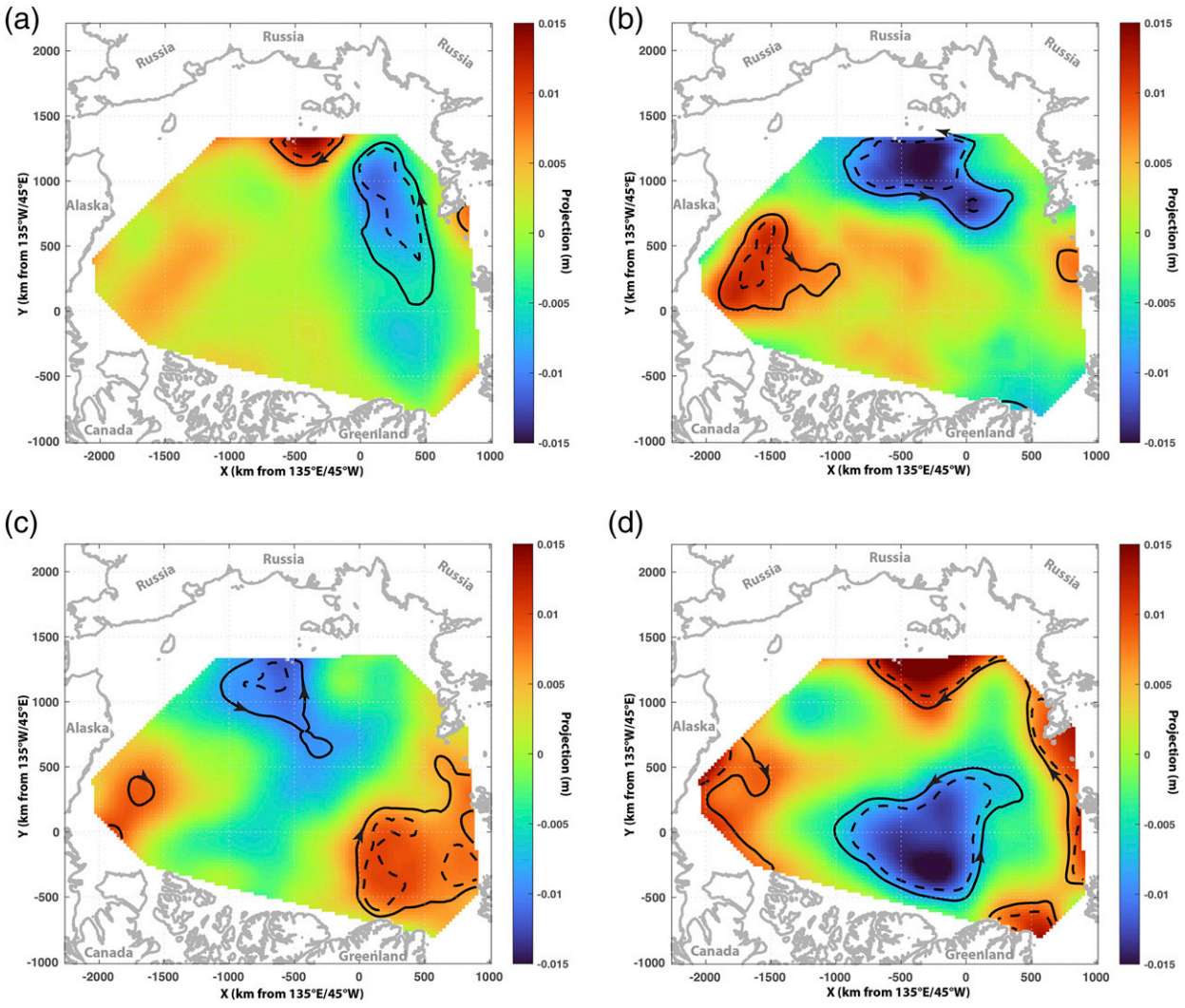

FIG. 13. Projections on the combined DH_{500} and DOT annual anomaly maps of the first-order responses of the AO with a time constant equal to 1 year and time lags of (a) zero lag ($R = 0.20$, $p = 0.17$), (b) 1 year ($R = 0.30$, $p = 0.03$), (c) 2 years ($R = 0.32$, $p = 0.02$), and (d) 3 years ($R = 0.23$, $p = 0.09$). The regions for which the correlation between the AO and the combined DH/DOT maps are significant at the 95% (97.5%) level are enclosed by solid (dashed) black contour lines.

averages in the latter half of the 1980s are a little higher than in the winter averages. The lagged first-order response to the AO is the blue line in Fig. 14.

As discussed with respect to Fig. 7, PC1 of the EWG period (green) and the combined "h" period (magenta) are virtually the same in the EWG period from 1950 to 1989 and they show a modest correspondence with the lagged, first-order response of the AO from 1950 to 1980. PC1 for the satellite era (green after 2003) and PC2 for the combined h period (dashed magenta) are nearly identical to each other from 2003 to 2014, and are similar to PC1 of the combined period from 2004 to 2012 when the combined record PC1 does not decline as deeply as the satellite period PC1 and actually begins to increase. All three of these records show the sharp increase of the lagged first-order AO response about 2008–09 and the sharp decrease in 2011–12.

The PC1 time series by themselves have correlations with the lagged first-order AO of about 0.15–0.5, but these are not significant, e.g., with values of p factor typically from 0.1 to 0.4. However, if we include a surrogate representation of the PC values during the extreme excursion of the AO in 1989–95 we find correlations between the PC1 and the AO that are significant. For these surrogate PC1 values we take the A1 values (plus, open circle, asterisk, and filled circle symbols in Fig. 14 at year = 1993.75) from the correlation analysis of the EOF1s with the *Pargo* DH_{500} anomalies (Fig. 10). Doing this, the correlation of the AO with the EWG era PC1 is 0.41, with the satellite era PC1 it is 0.56, with the combined EWG and satellite periods PC1 it is 0.30, and with the combined EWG and satellite periods PC2 it is 0.28, and all are significant at better than the 95% level (Table 1). Overall, if we include the peak AO response of the early 1990s characterized by the *Pargo*

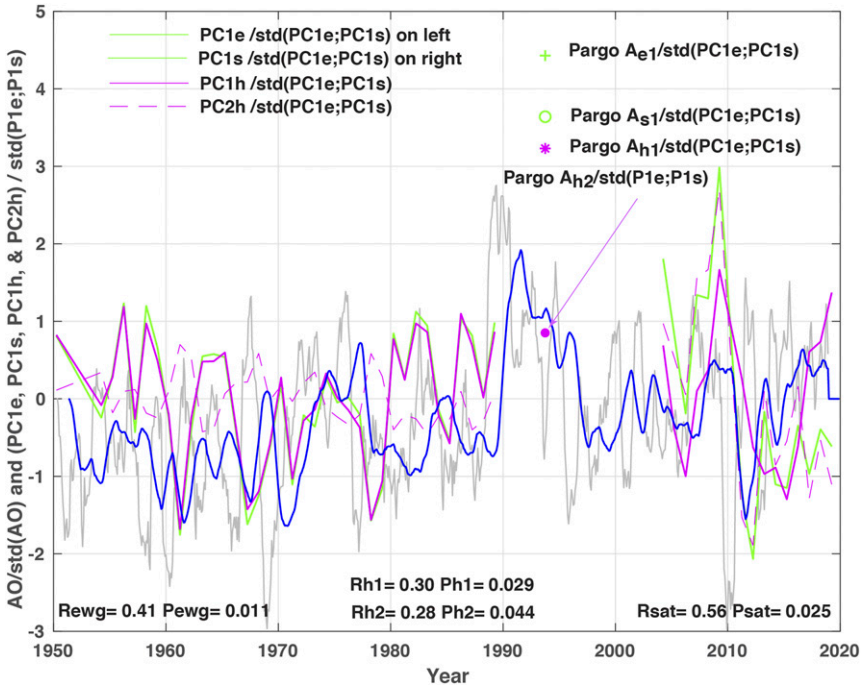

FIG. 14. The 1-yr running average AO (gray) with its first-order lagged response with time constant and lag equal to 1 year (blue). Also, PC1 time series plus *Pargo* EOF1 coefficients (Fig. 10) are shown for the EWG (denoted e), satellite (denoted s), and combined (denoted h) records. Surrogate PC1 coefficients for the *Pargo* DH_{500} anomalies are shown as labeled color-coded symbols.

data, the first-order AO response with 1-yr time constant and 1-yr delay can account for a significant fraction of the surface circulation variance embodied in the PC1.

8. Discussion

Associated with a positive shift in the winter AO starting in 1989, the Arctic Ocean has been mostly in a cyclonic surface circulation regime for the past 20–30 years characterized by increased Arctic Ocean average vorticity, a DOT trough on the Russian side of the Arctic Ocean, a less extensive but more intense Beaufort Gyre, and a cyclonic shift of the Transpolar Drift. EOF1 of DH_{500} from 1950 to 1993 and DOT from 2004 to 2019 capture this pattern.

The surface circulation becomes more cyclonic under positive AO and more anticyclonic under negative AO. We see that just as the 2004–19 average Arctic Ocean vorticity (Fig. 3b) is greater (more cyclonic) than the 1950–89 vorticity (Fig. 3a), the winter AO index is one standard deviation higher in 1989–2019 than it was prior to 1989, an increase that is statistically significant at the 99% level. Further, the interannual changes in DH and DOT associated with the AO increases in 1989 (Fig. 10) and 2007 (Fig. 11) show the development of the DOT depression on the Russian side of the Arctic Ocean and intensified Beaufort Gyre characteristic of the cyclonic mode, while the record AO decrease in 2010 (Fig. 12) shows the opposite, characteristic of reversion to the anticyclonic mode. Over the composite DH_{500} and DOT records 1950–2019 the principal component of EOF1 characterizing the cyclonic mode, like the AO (Fig. 9), shows greater positive and negative swings after 1989 than before (Figs. 7 and 14). And finally, the projection of a lagged first-order response of the winter AO (with time constant equal 1 year and lag equal 1 year) on DH_{500} and DOT, 1950–2019 (Fig. 13), shows a significant similarity to EOF1 and the dominant characteristics of the cyclonic mode. While correlations between the first EOF principal components and the first-order lagged response to the AO are not especially large, they are statistically significant (Table 1) if we include the virtual PC1s from the *Pargo* analysis of the response to the AO maximum in 1989–95 (Fig. 14). The correlation with the AO explains 41% of the variance in the pre-1990 PC1 and 56% of the variance in the post-1990 PC1. Over the combined record, correlation with the AO explains 30% in PC1 and 28% of the variance in the similar PC2. These fractions are reasonable in that the AO is a near-hemispheric index and not the sole determinant of Arctic atmospheric circulation.

TABLE 1. Correlations between the winter AO index and principal components of the Arctic Ocean surface height.

Principal component	Correlation *R*	*p* factor
EWG PC1	0.41	0.011
Satellite era PC1	0.56	0.025
Combined EWG/satellite PC1	0.30	0.029
Combined EWG/satellite PC2	0.28	0.044

There is the suggestion comparing pre- and post-1990 surface circulation that, likely associated with the plus one standard deviation shift in the AO (Fig. 9), the increase in mean vorticity (Fig. 3), and perhaps with a change in average ice conditions, the modes of surface circulation have changed somewhat (Figs. 4 and 5). EOF1 prior to 1990 shows a depression on the Russian side of the Arctic Ocean concentrated in the Makarov Basin extending to the North Pole (Fig. 4a). During the satellite era, 2004–19, EOF1 (Fig. 5a) is marked by a trough that wraps farther around the Russian side of the Arctic Ocean from the Fram Strait eastward in an arc across the southern Makarov Basin to the western Beaufort Sea. This trough is offset by doming centered over the North Pole producing a dipole pattern. The EOF2 patterns are also slightly different pre and post-1990. EOF2 for both the pre-1990 data (Fig. 4b) and post-1990 data (Fig. 5b) show a Canada Basin versus Nansen–Amundsen Basin dipole character with a low on the Nansen–Amundsen side and a high on the Canada side. However, the Canada-side positive center of action is spread farther south into the Beaufort Sea in the post-1990 DOT EOF2 (Fig. 5b) than in the pre-1990 EOF2 (Fig. 4b). In the combined record (Figs. 6a,b) EOF1 resembles EOF1 of the pre-1990 record and EOF2 resembles the EOF1 of the post-1990 record. This split is a reflection of the change in modes of circulation after 1990 as the combined record analysis tries to account for the change in EOF1. The combined PC2 and PC1 vary together until 2012–13, and overall they account for 60% of the variance in the combined DH_{500} and DOT records. This, along with the change in EOF1 reflected in EOF1 and EOF2 of the combined record, would increase the DOT gradient between the cyclonic and anticyclonic cells of the cyclonic mode and thus the strength of the Transpolar Drift (Morison et al. 2012). Overall the results suggest a regime shift in the exact manner of Arctic Ocean surface circulation variability with an average cyclonic circulation shift in the last 30 years (Fig. 3).

The surface circulation changes of the cyclonic mode overlie an inherently cyclonic deep circulation. Absent wind forcing, the Arctic Ocean would have a fjord-like cyclonic circulation due to the throughflow of relatively fresh Pacific Water driven by the greater steric sea surface height of the Pacific relative the Atlantic (Steele and Ermold 2007). The outflow of Pacific Water mixed with runoff and Atlantic Water requires an Atlantic Water inflow to conserve mass and salt. Conservation of potential vorticity would require the cyclonic circulation of both the Atlantic and Pacific derived water with Atlantic Water inflow deep on the east side of Fram Strait, outflow of Pacific-derived Water near the surface on the west side of Fram Strait and Canadian Archipelago, and Atlantic Water sliding beneath Pacific-derived Water along the Transpolar Front. In actuality, once below the effect of surfacing forcing, the Atlantic Water is topographically controlled by conservation of potential vorticity (Nøst and Isachsen 2003; Timmermans and Marshall 2020) and eddy–topography interaction (Holloway 1987, 1996), and it circulates cyclonically around the Eurasian, Makarov, and Canada Basins (Dickson et al. 2000; Rudels 2012). Furthermore, the strength of this underlying cyclonic circulation, at least in the Eurasian Basin, increases with the strength of the Atlantic Water inflow according to a climate response function driven by cyclonic winds in the Greenland Sea (Muilwijk et al. 2019).

The underlying cyclonic circulation is mainly opposed by anticyclonic wind-driven surface circulation, but the cyclonic mode in surface circulation represents a partial reversal of this opposition that is played out in the position of the Transpolar Front across the Makarov Basin. The Beaufort high in average atmospheric pressure (Fig. 8a) drives an anticyclonic near-surface average ocean circulation that is counter to the inherently cyclonic deeper circulation (Timmermans and Marshall 2020; Zhang and Steele 2007). There is a tendency for average cyclonic surface circulation in the southern parts of the deep Eurasian Basin (Figs. 2 and 6d) owing to an average low in atmospheric pressure extending from the Nordic seas up across the Barents Sea (Fig. 8a) and to the presence of the inflowing Atlantic Water near the surface (Nøst and Isachsen 2003). At the surface, the border between the anticyclonic and anticyclonic regions varies across the Amundsen and Makarov basins. Under positive AO, cyclonic atmospheric forcing extends across the Eurasian to the Makarov Basins (Fig. 8b), cyclonic surface circulation spreads across the Eurasian Basin and into (Figs. 2b, 4a, 6a) and across (Fig. 5a) the Makarov Basin, and the Transpolar Front shifts toward North America (Fig. 3), hallmarks of the cyclonic mode that are complementary to the underlying cyclonic circulation. Under a positive AO, the underlying cyclonic circulation in the Arctic Basin is further reinforced by increased Atlantic Water inflow due to increased wind forcing in the Nordic seas (Muilwijk et al. 2019; Nøst and Isachsen 2003).

On the other hand, when the AO is negative, atmospheric pressure rises over the Eurasian and Makarov basins (Fig. 8b), the Makarov Basin and Eurasian Basin surface circulation becomes anticyclonic (negative PC1 times the EOF1 of Figs. 2a, 4a, and 6a) counter to the underlying cyclonic circulation, and the Transpolar Front swings toward Russia, hallmarks of what might be called the anticyclonic mode.

Comparison of our analysis with other studies suggests the cyclonic mode represents a complex of changes dependent on increased AO. These include studies of changes in surface and Atlantic Water circulation with the AO, the regime shift in AO and ocean response after 1990, and consequent changes in the flux of ice from the Arctic Ocean. Most of these studies have focused on the response of the sea ice to changes in the AO or the closely correlated North Atlantic Oscillation (NAO). Therefore, it is important to point out the close relation between ice velocity and the upper-ocean geostrophic velocity that results from the balance of Coriolis force and the cross gradient of DH_{500} or DOT (e.g., vectors in Figs. 11 and 12). The geostrophic velocity of the ice resulting from the gradient in DOT is the same as the geostrophic velocity of the upper-ocean. Under relatively short but intense wind events, the wind stress causes the ice to move at about 2% and 20° to the right of the wind velocity (Nansen 1902; Thorndike and Colony 1982), but averaged over many wind storms and quiet periods, and at sufficiently large horizontal scales, internal ice stress is of reduced importance in the deep basins far from shore, and ice velocity closely resembles upper-ocean geostrophic velocity (Kwok and Morison 2017).

We find that to understand the response of Arctic Ocean surface circulation to the AO it is critical to account for latency in the spin up of the ocean in response to interannual changes in wind forcing. A number of studies have looked at impact of the AO or NAO on ice motion, export and volume (Dickson et al. 2000; Hilmer and Jung 2000; Kwok 2000; Morison et al. 2018b; Rigor and Wallace 2004; Rigor et al. 2002; Williams et al. 2016; Zhang et al. 2000; Zhang et al. 2003). Morison et al. (2018b) observe in annual 2005–15, springtime hydrographic sections across the North Pole along 90°W–90°E that in years of high winter AO, the transpolar Front is shifted toward North America. Dickson et al. (2000) find an increase in ice flux from the Arctic Ocean with increased NAO. Kwok (2000) examined monthly composites of ice motion 1978–96 for different levels of the NAO. Similarly, Zhang et al. (2003) show composites of simulated ice motion, ice thickness, and related ocean properties for high and low phases of the AO. Both studies find the high NAO/AO composite ice export through Fram Strait is enhanced, and the high AO/NAO composite ice velocity anomaly is essentially cyclonic surface circulation around the periphery of the Arctic Basin, much as Armitage et al. (2018) find for geostrophic surface current under positive AO and similar to our projection of zero-lag AO on DH_{500} and DOT (Fig. 13a). These composites of simultaneous surface circulation and AO, similar to Fig. 13a, do not capture the essential element of the first EOF of DH_{500} and DOT (Figs. 4a, 5a, 6a) that is the cyclonic surface circulation on the Russian side of the Arctic Ocean as illustrated by the projection of 1-yr-lagged AO on DH_{500} and DOT (Fig. 13b). A finely tuned analysis of the temporal response of the ocean to the AO is beyond the scope of this study using ocean data that is annual at best, but our results show that an AO response lagged and smoothed with time scales of at least a year (Fig. 13b) is needed to represent the key features of the fundamental, EOF1, mode of surface circulation variability (Figs. 4a, 5a, 6a).

This work shares with a number of others the overarching idea that the early 1990s marked a regime shift in the behavior of the Arctic Ocean. Rigor et al. (2002), in one of the first studies of the relation between the AO and ice extent, take account of the latency between the AO and September ice extent (SIE), which they find is negatively correlated with the previous winter AO due to advection of new ice away from the East Siberian coastal areas, keeping the ice cover thin over large areas on the Russian side of the Canada Basin. The increased export of ice out of the Arctic Ocean during the 1990s period of high AO reduced the amount of resident thick multiyear ice and was critical in shifting the Arctic Ocean toward a more seasonal sea ice regime (Lindsay and Zhang 2005; Rigor and Wallace 2004). Similar to Rigor et al. (2002), Williams et al. (2016), in a study using a Lagrangian back-trajectory model, find that the integrated winter anomaly of ice advected away from the Alaskan and Eurasian coastline is correlated with the September sea ice extent. The winter export anomaly is in turn correlated with the winter AO, and consequently September sea ice extent is negatively correlated with the AO. However, recognizing the fundamental positive shift in the AO in the early 1990s (Fig. 9), they also find that prior to 1993, the negative correlation between the AO and SIE was not strong. They speculate that this was because thicker ice in earlier years limited the influence of the AO on ice motion and argue that this is why including years prior to 1993 in analyses produces insignificant correlations between the AO and sea ice extent (Holland and Stroeve 2011). This raises the idea that the differences we see in between the EWG-era 1950–89 EOF1 (Fig. 4a) and satellite era 2004–19 EOF1 (Fig. 5a) could be due to the substantial changes in ice extent, thickness and strength. One can certainly imagine that the ocean would respond more readily to small changes in the AO since the ice has become thinner and less extensive in the early 1990s.

Other work that recognizes the regime shift in the AO (or NAO) and its effect on ice includes Zhang et al. (2000). Their simulations comparing the high NAO period (1989–96) to the prior low NAO period (1979–88) show ice is lost preferentially from the eastern Arctic as opposed to the western Arctic in what they term a dipolar East–West Arctic anomaly pattern (EWAAP), ice export is increased, and net Arctic Ocean ice volume is decreased 20%. Tucker et al. (2001) show ice draft and inferred thickness as measured by submarines 1992–94 decreased relative to 1985–88 under the shift to a more positive AO and argue this was likely due to dynamic processes associated with a substantial decrease in the western extent of the Beaufort Gyre and a cyclonic shift in and intensification of the Transpolar Drift (Tucker et al. 2001). Steele and Boyd (1998) compare ice velocity fields averaged during a low AO period 1979–87 and the high AO period 1988–96, and also find the Beaufort Gyre decreased in western extent and the Transpolar Drift axis shifted cyclonically.

Several studies of changes in the atmosphere (Hilmer and Jung 2000; Wang et al. 2009; Zhang et al. 2004) offer interesting comparisons to our study. Hilmer and Jung (2000) compare Fram Strait ice export and the NAO from 1958 to 1997. They find ice export uncorrelated with the NAO until 1977, but significantly positively correlated thereafter. They show that this change was due to a shift in the low-pressure center of action of the NAO to the east so as to present a dipole pattern straddling Fram Strait that drives ice export through the strait under positive NAO. The pattern is similar to our projection of the AO with zero-lag on DH_{500} and DOT (Fig. 13a) with high DOT west of Fram Strait and low DOT east of Fram Strait in a relation that will also drive southward geostrophic ice export.

A related comparison comes from Wang et al. (2009) who find that record lows in summer sea ice extent between 1995 and 2008 are correlated with a positive summer dipole anomaly (DA) pattern, the second EOF of atmospheric sea level pressure (SLP). The winter DA pattern is a high in the Eurasian Basin and low in Canada Basin. The summer DA pattern is essentially minus the winter DA pattern turned 90° clockwise, low toward the Russian side and high toward the Canadian side, so that it drives ice drift from Bering Strait to Fram Strait. Wang et al. (2009) find the greatest ice loss occurs when both the AO and DA are positive. It is noteworthy that the second EOF of EWG DH_{500} (Fig. 4b) strongly resembles the negative of the winter DA pattern with a low in the Eurasian Basin and high in the Canada Basin. The second EOF of satellite DOT (Fig. 5b) resembles a pattern part way between the negative of

the winter DA and the summer DA, with a ridge extending eastward along the Canadian Archipelago and a trough spread from Fram Strait over and around the Eurasian Basin margin. These, like the positive summer DA, would enhance geostrophic ice export through Fram Strait.

Smedsrud et al. (2017) find results consistent with Wang et al. (2009) using a record of Fram Strait ice area export extended back 80 years using an ice export proxy based on the SLP difference across Fram Strait. They find increased ice area export between the 1970s and 2014 with a high correlation with the DA (Smedsrud et al. 2017). In situ observations including ice draft since the early 1990s indicate ice volume export, as opposed to ice area export, had a negative trend from 1992 to 2014 due to declining basin ice thickness (Spreen et al. 2020). Though Smedsrud et al. (2017) do not directly address correlations of ice export with the AO, their extensive ice export record shows increased ice export in 2007–09, a period of increased AO (Fig. 11), decreased ice export in 2010 during the record low AO (Fig. 12), and increasing ice export after 2010 when the AO increased, suggesting a positive correlation of ice export with the AO.

Similarly, though the record of ice export from winter of 1990–91 to winter of 2006–07 does not show a statistically significant trend (Kwok 2009), it does demonstrate a correlation with the AO. Kwok's (2009) ice export is a maximum in 1994–95 after the 5-yr average record high in AO then declines through the 1990s reaching near the pre-1989 value around 2003 when the AO and ocean conditions at the Pole reach pre-1989 conditions (Morison et al. 2006) and then increases in the 2006–07 winter with an increase in the AO (Figs. 9 and 11).

Zhang et al. (2004), based on analysis of data from the 1950s to 2003, find the cyclone activity index (CAI), a measure of the number of cyclones in a region, in the Arctic Ocean is strongly correlated with the AO. Like the AO, the CAI increased substantially during 1988–90 and was high through most of the 1990s. At the same time midlatitude CAI decreased. This correspondence between the AO and CAI relates to an open question regarding the AO spinup of the cyclonic mode over the last three decades. Namely, is cyclonic spinup more the result of the mean cyclonic pattern wind field of the AO (Fig. 8b), which it indeed resembles, or is it the result of the advection of more atmospheric cyclones into the Arctic by the action of the increased AO? This question is open, but it is safe to say neither the mean AO pattern nor associated enhanced cyclone activity would lead to more anticyclonic circulation in the Arctic Ocean.

This brings us to a number of studies that have argued that increasingly anticyclonic circulation in the Arctic Ocean in recent decades have led to increased freshwater storage, mainly through Ekman pumping of near surface low salinity water into the Beaufort Gyre (Hofmann et al. 2015; McPhee et al. 2009; Proshutinsky et al. 2015, 2009). If the conclusions of these and related studies as to circulation becoming more anticyclonic and increasing freshwater storage were confined to consideration of the Beaufort Sea, they would agree with our results.

Although the Beaufort Gyre is not the center of action for the EOF1 of either the EWG DH_{500}, satellite DOT, or combined DH_{500} and DOT records, it does appear as a dome adjacent to the larger Russian-side trough in EOF1 (Fig. 6a) of the combined DH_{500} and DOT record. As a consequence, after the AO increase in 2007 while the Russian-side trough deepened and lost freshwater, the Beaufort Gyre strengthened and gained virtually the same amount of freshwater (Fig. 11c; Morison et al. 2012). The cyclonic mode associated with rising AO is a Beaufort Sea versus Russian-side dipole where strengthening and freshening of the Beaufort Gyre is balanced by salinization and deepening of the Russian-side trough (Morison et al. 2012).

9. Conclusions

For 70 years, the dominant mode of variability in Arctic Ocean surface circulation, exemplified by the first EOF of sea surface height, has been a dipole pattern dominated by a low in sea surface height with cyclonic surface circulation on the Russian side of the deep Arctic Ocean and an opposing high with anticyclonic surface circulation on the Canadian Archipelago side. Under positive AO, the dominant mode of variation in its positive (cyclonic) phase causes extension of the Eurasian Basin cyclonic flow westward across the Makarov Basin, and a tightening of the Beaufort Gyre. Under negative AO, the dominant mode in the negative phase leads to an expansion of the anticyclonic Beaufort Gyre and a contraction of the cyclonic flow on the European side.

There is a link between the AO and the cyclonic mode. We see this at the interannual scale with the shift to the cyclonic mode under substantial increases of the AO in the early 1990s and in 2007–08. We see it as a retreat of the cyclonic mode under a short shift to record minimum AO in 2010. The principal component of EOF1 corresponding to the intensity of the cyclonic mode is positively correlated with a first-order response to the AO with time constant of 1 year and a lag of 1 year.

In response to the one standard deviation shift in the average AO starting in 1989–90, the first EOF and cyclonic mode have changed slightly, with tendencies toward increased variation across the resulting dipole pattern and greater shifts in the orientation of the Transpolar Drift and the pathways of freshwater. The seeming greater responsiveness to the AO may be related to the shift to less multiyear ice and related reduction in ice volume and strength over the same time.

Setting aside discussion of ocean modes of variability, not one of the studies of the response of the Arctic Ocean to increasing AO cited above found that ice or freshwater export decreased with increasing AO. Just the opposite, they found that elevated AO, which has characterized the last 30 years, leads to greater ice and associated freshwater export. This is completely consistent with the Arctic Ocean overall being in a more cyclonic state as evidenced by the positive change in basin average vorticity (Fig. 3). The same Ekman dynamics that drive convergence of freshwater and sea ice into an increasingly anticyclonic (decreasing vorticity) gyre, cause freshwater and sea ice to diverge from an increasingly cyclonic (increasing vorticity) gyre. The Arctic Ocean's increased vorticity (Fig. 3) and increased AO (Figs. 9 and 14),

and increased ice export (references above) are only consistent with a more cyclonic circulation regime and less tendency to store freshwater in the Arctic Ocean.

The cyclonic mode is important for several reasons. In as much as the cyclonic mode is related to the AO, it is related to climate change because rising AO has been argued to be a characteristic of global warming (Choi et al. 2010; Fyfe et al. 1999; Gillett et al. 2002; Miller et al. 2006; Rind et al. 2005; Shindell et al. 1999). As discussed above, the impact of the AO and cyclonic mode on the ice cover is significant. The cyclonic mode leads to more ice export from the marginal seas causing a negative correlation between summer ice extent and the previous winter AO (Rigor et al. 2002; Williams et al. 2016). This in turn potentially leads to increasing stratification and reduction in global thermohaline overturning circulation in the Nordic seas.

The cyclonic mode may be most important as part of a complex of overall circulation changes that could melt large amounts of sea ice. It has long been appreciated that relatively small increases in Atlantic Water heat flux to the surface (e.g., $2\,W\,m^{-2}$ average over the Arctic Ocean) could drastically decrease ice thickness (Maykut and Untersteiner 1971), but the stratification of the cold-halocline layer between the mixed layer and the Atlantic Water has effectively isolated the Atlantic Water heat at depth except near the Fram Strait and Barents Sea inflows (Gorshkov 1983) where it enhances bottom melting of sea ice (Ivanov et al. 2016). Several mechanisms maintain the cold halocline (Aagaard et al. 1981; Steele and Boyd 1998), but an important one (Rudels et al. 1996) involves the injection of cold shelf water freshened by Eurasian runoff into the halocline of the eastern Eurasian Basin. The cyclonic mode diverts Eurasian runoff eastward (Morison et al. 2012), weakening the cold halocline layer (Steele and Boyd 1998), and allowing Atlantic Water heat to reach the surface and melt the ice cover from below. The impact of this is heightened by the increase Atlantic Water inflow volume (Dickson et al. 2000; Muilwijk et al. 2019; Nøst and Isachsen 2003) and temperature (Dickson et al. 2000; Swift et al. 1997) with increased AO or NAO. Given the elevated state of the AO and prevalence of the cyclonic mode, it is understandable that we have seen a greater role for Atlantic Water heat in ice loss (Polyakov et al. 2017) and a threefold increase in Atlantic Water heat flux to the mixed layer since 2007 (Polyakov et al. 2020). The cyclonic mode complex of changes thus includes reduction of the sea ice cover through Atlantic Water heat flux and thus initiation of sea ice–albedo feedback on climate.

In spite of the cyclonic mode's importance, our in situ observing system is not well configured to detect it, and we would argue a concentration of measurements in the Beaufort Sea has led to an anticyclonic surface circulation centered view of the Arctic Ocean. In winter and early spring, the in situ observing system usually consists exclusively of instrumented drifting buoys. In March of 2019, the end of the period studied here, the buoy array included International Arctic Buoy Program (IABP) surface drifters measuring surface air temperature and pressure. These drifters were mostly in the Beaufort Sea and Transpolar Drift. Six Ice Tethered Profilers (ITP) measuring profiles of temperature and salinity were all in the Beaufort Sea. Three UpTempO near-surface temperature profile buoys and three Weather–Waves-Ice Mass Balance–Ocean (WIMBO) buoys were also in the Beaufort Sea. The ocean moorings of the Beaufort Gyre Exploration Project were in place in the Beaufort Sea. With the exception of a few IABP surface drifter tracks, there were no in situ observations in the region of dominant DOT variability. This is not an unusual situation. The Russian side of the ocean, and particularly the Makarov Basin, is a region that is difficult to reach to deploy drifting buoys and to conduct hydrographic surveys. Further, ice and drifting buoys tend to converge in an anticyclonic feature like the Beaufort Gyre and diverge from cyclonic circulation like that in the Makarov Basin under the cyclonic mode. Most of the time the hallmark ocean conditions of the cyclonic mode have been unobserved by our in situ oceanographic measurements.

Whereas most present in situ observations miss the dominant modes of variability, satellite altimetry covers the entire Arctic Ocean. For example, the new *ICESat-2* altimetry reveals that the ocean surface circulation was in an increasingly cyclonic mode in 2019. The *ICESat-2* SSH anomaly relative to the *CryoSat-2* 2011–15 mean sea surface was −20 cm on the Russian side of the Arctic Ocean, implying a relatively cyclonic mode. To better observe the surface circulation of the cyclonic mode in the future, we can rely on altimeters such as *ICESat-2* and *CryoSat-2* and the mass change observations of GRACE Follow-On.

However, to understand changes below the surface such as the Atlantic Water heat flux to the ice, we should be making more in situ observations in the critical areas around the Transpolar Front, in the Makarov Basin, and eastern Eurasian Basin where change is most extreme and likely has the largest effect (e.g., Morison et al. 2018b).

Acknowledgments. Support for this work has been provided for J. Morison, Dickinson, Andersen, and D. Morison by NASA Grants NNX13AP72G, NWX15AE27G, NNX16AF18G, and 80NSSC20K0955; ONR Grants N00014-15-1-2295 and N00014-19-1-2555; and NSF Grant ARC-0856330. Peralta-Ferriz was supported by NASA Grants NNX16AF18G and 80NSSC20K0763. Dewey was supported by ONR Grant N00014-15-1-2295. Rigor was supported by contributors to the U.S. Interagency Arctic Buoy Program, which include NASA Grant 80NSSC18K0872; National Ice Center Grant NA15OAR4320063; NOAA Grant NA15OAR4310154; NSF Grants OPP-1951762 and PLR-1602533; and ONR Grant N00014-20-1-2207. Guthrie was supported by ONR Grant N00014-16-2379.

Data availability statement. The EWG dynamic height data are available at a number of locations including NASA Earthdata at NSIDC: https://cmr.earthdata.nasa.gov/search/concepts/C1386246245-NSIDCV0.html and by ftp at ftp://sidads.colorado.edu/pub/DATASETS/NOAA/G01961. The *ICESat* DOT data for the Arctic Ocean and Nordic seas are taken from *ICESat* altimetry from GLA15 Version 34 from the NASA Distributed Active Archive Center at the National

Snow and Ice Data Center (https://nsidc.org/data/icesat/data.html). For the *ICESat* DOT in the Sub-Arctic Seas, the sea state bias correction of Morison et al. (2018a) was applied using significant wave height data from the European Center for Medium Range Weather Forecasting (ECMWF) ERA-20C Ocean Wave analysis: https://apps.ecmwf.int/datasets/data/era20c-wave-daily/type=an/. *CryoSat-2* DOT data for the Arctic Ocean are taken directly from the Synthetic Aperture Radar (SAR) Interferometric Radar ALtimeter (SIRAL) instrument on *CryoSat-2* available through ESA's data portal (URL: https://earth.esa.int). The 2011–17 the Nordic seas *CryoSat-2* data (Fig. 11) come from the Radar Altimeter Database System (RADS, http://rads.tudelft.nl/rads/rads.shtml). The Submarine Arctic Science Program (SCICEX) 1993 *Pargo* DH data are calculated from CTD data available at the National Ocean Data Center sites for SCICEX 1993 surface casts (https://www.nodc.noaa.gov/archive/arc0001/0000516/) and Submarine Ship-launched eXpendable CTD (SSXCTD) profiles (https://www.nodc.noaa.gov/archive/arc0021/0000568/) through the National Snow and Ice Data Center SCICEX data portal: (file://localhost/ (https/::nsidc.org:scicex:data_inventory.html). Monthly averages of the AO index are taken in tabular form from the NOAA NCEP: https://www.cpc.ncep.noaa.gov/products/precip/CWlink/daily_ao_index/monthly.ao.index.b50.current.ascii.table.

REFERENCES

Aagaard, K., and P. Greisman, 1975: Toward new mass and heat budgets for the Arctic Ocean. *J. Geophys. Res.*, **80**, 3821–3827, https://doi.org/10.1029/JC080i027p03821.

——, L. K. Coachman, and E. Carmack, 1981: On the halocline of the Arctic Ocean. *Deep-Sea Res.*, **28A**, 529–545, https://doi.org/10.1016/0198-0149(81)90115-1.

Alkire, M. B., J. Morison, and R. Andersen, 2015: Variability in the meteoric water, sea-ice melt, and Pacific water contributions to the central Arctic Ocean, 2000–2014. *J. Geophys. Res. Oceans*, **120**, 1573–1598, https://doi.org/10.1002/2014JC010023.

Anderson, L. G., and Coauthors, 1994: Water masses and circulation in the Eurasian Basin - Results from the Oden 91 expedition. *J. Geophys. Res.*, **99**, 3273–3283, https://doi.org/10.1029/93JC02977.

Armitage, T. W. K., S. Bacon, and R. Kwok, 2018: Arctic sea level and surface circulation response to the Arctic Oscillation. *Geophys. Res. Lett.*, **45**, 6576–6584, https://doi.org/10.1029/2018GL078386.

Carmack, E. C., R. W. Macdonald, R. G. Perkin, F. A. McLaughlin, and R. J. Pearson, 1995: Evidence for warming of Atlantic water in the southern Canadian basin of the Arctic Ocean: Results from the Larsen-93 expedition. *Geophys. Res. Lett.*, **22**, 1061–1064, https://doi.org/10.1029/95GL00808.

——, and Coauthors, 1997: Changes in temperature and tracer distributions within the Arctic Ocean: Results from the 1994 Arctic Ocean section. *Deep-Sea Res. II*, **44**, 1487–1502, https://doi.org/10.1016/S0967-0645(97)00056-8.

Choi, D.-H., J.-S. Kug, W.-T. Kwon, F.-F. Jin, H.-J. Baek, and S.-K. Min, 2010: Arctic Oscillation responses to greenhouse warming and role of synoptic eddy feedback. *J. Geophys. Res.*, **115**, D17103, https://doi.org/10.1029/2010JD014160.

Dewey, S., J. H. Morison, and J. Zhang, 2017: An edge-referenced surface fresh layer in the Beaufort Sea seasonal ice zone. *J. Phys. Oceanogr.*, **47**, 1125–1144, https://doi.org/10.1175/JPO-D-16-0158.1.

Dickson, R. R., and Coauthors, 2000: The Arctic Ocean response to the North Atlantic Oscillation. *J. Climate*, **13**, 2671–2696, https://doi.org/10.1175/1520-0442(2000)013<2671:TAORTT>2.0.CO;2.

Fyfe, J. C., G. J. Boer, and G. M. Flato, 1999: The Arctic and Antarctic Oscillations and their projected changes under global warming. *Geophys. Res. Lett.*, **26**, 1601–1604, https://doi.org/10.1029/1999GL900317.

Giles, K. A., S. W. Laxon, A. L. Ridout, D. J. Wingham, and S. Bacon, 2012: Western Arctic Ocean freshwater storage increased by wind-driven spin-up of the Beaufort Gyre. *Nat. Geosci.*, **5**, 194–197, https://doi.org/10.1038/ngeo1379.

Gillett, N. P., M. R. Allen, and K. D. Williams, 2002: The role of stratospheric resolution in simulating the Arctic Oscillation response to greenhouse gases. *Geophys. Res. Lett.*, **29**, 1500, https://doi.org/10.1029/2001GL014444.

Gore, A., and D. Belt, 1997: An Arctic breakthrough. *Natl. Geogr. Mag.*, **191**, 36–59.

Gorshkov, S. G., 1983: *Arctic Ocean*. Vol. 3, *World Ocean Atlas*, Pergamon Press, 189 pp.

Gudkovich, Z. M., 1961: Relation of the ice drift in the Arctic Basin to ice conditions in the Soviet Arctic seas (in Russian). *Tr. Okeanogr. Kom. Akad. Nauk SSSR*, **11**, 14–21.

Hilmer, M., and T. Jung, 2000: Evidence for a recent change in the link between the North Atlantic oscillation and Arctic sea ice export. *Geophys. Res. Lett.*, **27**, 989–992, https://doi.org/10.1029/1999GL010944.

Hofmann, E., M. St. John, and H. M. E. Benway, 2015: A science plan for a collaborative international research program on the coupled North Atlantic-Arctic system. Planning Workshop for an Int. Research Program on the Coupled North Atlantic-Arctic System, Arlington, VA, Old Dominion University, 37 pp., ttps://doi.org/10.1575/1912/7776.

Holland, M. M., and J. Stroeve, 2011: Changing seasonal sea ice predictor relationships in a changing Arctic climate. *Geophys. Res. Lett.*, **38**, L18501, https://doi.org/10.1029/2011GL049303.

Holloway, G., 1987: Systematic forcing of large-scale geophysical flows by eddy-topography interaction. *J. Fluid Mech.*, **184**, 463–476, https://doi.org/10.1017/S0022112087002970.

——, 1996: Neptune effect: Statistical mechanical forcing of ocean circulation. *Stochastic Modelling in Physical Oceanography*, R. Adler, P. Müller, and B. Rozovskii, Eds., Birkhäuser, 207–219.

Ivanov, V. V. Alexeev, N. V. Koldunov, I. Repina, A. B. Sando, L. H. Smedsrud, and A. Smirnov, 2016: Arctic Ocean heat impact on regional ice decay: A suggested positive feedback. *J. Phys. Oceanogr.*, **46**, 1437–1456, https://doi.org/10.1175/JPO-D-15-0144.1.

Kwok, R., 2000: Recent changes in Arctic Ocean sea ice motion associated with the North Atlantic Oscillation. *Geophys. Res. Lett.*, **27**, 775–778, https://doi.org/10.1029/1999GL002382.

——, 2009: Outflow of Arctic Ocean sea ice into the Greenland and Barents Seas: 1979–2007. *J. Climate*, **22**, 2438–2457, https://doi.org/10.1175/2008JCLI2819.1.

——, and J. Morison, 2011: Dynamic topography of the ice-covered Arctic Ocean from *ICESat*. *Geophys. Res. Lett.*, **38**, L02501, https://doi.org/10.1029/2010GL046063.

——, and ——, 2016: Sea surface height and dynamic topography of the ice-covered oceans from CryoSat-2: 2011–2014. *J. Geophys. Res. Oceans*, **121**, 674–692, https://doi.org/10.1002/2015JC011357.

——, and ——, 2017: Recent changes in Arctic sea ice and ocean circulation. *US CLIVAR Variations*, Vol. 15, No. 3, U.S. CLIVAR Project Office, Washington, DC, 1–6, https://doi.org/10.5065/D6833QQP.

Lindsay, R. W., and J. Zhang, 2005: The thinning of Arctic sea ice, 1988–2003: Have we passed a tipping point? *J. Climate*, **18**, 4879–4894, https://doi.org/10.1175/JCLI3587.1.

Maykut, G. A., and N. Untersteiner, 1971: Some results from a time-dependent thermodynamic model of sea ice. *J. Geophys. Res.*, **76**, 1550–1575, https://doi.org/10.1029/JC076i006p01550.

McAdoo, D. C., S. L. Farrell, S. Laxon, A. Ridout, H. J. Zwally, and D. Yi, 2013: Gravity of the Arctic Ocean from satellite data with validations using airborne gravimetry: Oceanographic implications. *J. Geophys. Res. Oceans*, **118**, 917–930, https://doi.org/10.1002/jgrc.20080.

McLaughlin, F. A., E. C. Carmack, R. W. Macdonald, and J. K. B. Bishop, 1996: Physical and geochemical properties across the Atlantic/Pacific water mass front in the southern Canadian basin. *J. Geophys. Res.*, **101**, 1183–1197, https://doi.org/10.1029/95JC02634.

McPhee, M. G., A. Proshutinsky, J. Morison, M. Steele, and M. Alkire, 2009: Rapid change in freshwater content of the Arctic Ocean. *Geophys. Res. Lett.*, **36**, L10602, https://doi.org/10.1029/2009GL037525.

Miller, R. L., G. A. Schmidt, and D. T. Shindell, 2006: Forced annular variations in the 20th century Intergovernmental Panel on Climate Change Fourth Assessment Report models. *J. Geophys. Res.*, **111**, D18101, https://doi.org/10.1029/2005JD006323.

Morison, J. H., M. Steele, and R. Andersen, 1998: Hydrography of the upper Arctic Ocean measured from the nuclear submarine USS Pargo. *Deep-Sea Res. I*, **45**, 15–38, https://doi.org/10.1016/S0967-0637(97)00025-3.

——, K. Aagaard, and M. Steele, 2000: Recent environmental changes in the Arctic: A review. *Arctic*, **53**, 359–371, https://doi.org/10.14430/arctic867.

——, M. Steele, T. Kikuchi, K. Falkner, and W. Smethie, 2006: Relaxation of central Arctic Ocean hydrography to pre-1990s climatology. *Geophys. Res. Lett.*, **33**, L17604, https://doi.org/10.1029/2006GL026826.

——, R. Kwok, C. Peralta-Ferriz, M. Alkire, I. Rigor, R. Andersen, and M. Steele, 2012: Changing Arctic Ocean freshwater pathways. *Nature*, **481**, 66–70, https://doi.org/10.1038/nature10705.

——, ——, S. Dickinson, D. Morison, C. Peralta-Ferriz, and R. Andersen, 2018a: Sea state bias of *ICESat* in the sub-Arctic seas. *IEEE Geosci. Remote Sens. Lett.*, **15**, 1144–1148, https://doi.org/10.1109/LGRS.2018.2834362.

——, and Coauthors, 2018b: The North Pole region as an indicator of the changing Arctic Ocean: The Need for sustaining observations. *Arctic*, **71** (5), 1–5, https://doi.org/10.14430/arctic4601.

Muilwijk, M., and Coauthors, 2019: Arctic Ocean response to Greenland sea wind anomalies in a suite of model simulations. *J. Geophys. Res. Oceans*, **124**, 6286–6322, https://doi.org/10.1029/2019JC015101.

Nansen, F., 1902: The oceanography of the North Polar Basin. *The Norwegian North Polar Expedition 1893-1896, Scientific Results*, Vol. 3, Longmans, Green, and Company, 427 pp.

Neumann, G., and W. J. Pierson, 1966: *Principles of Physical Oceanography*. Prentice-Hall, 545 pp.

North, G. R., T. L. Bell, R. F. Cahalan, and F. J. Moeng, 1982: Sampling errors in the estimation of empirical orthogonal functions. *Mon. Wea. Rev.*, **110**, 699–706, https://doi.org/10.1175/1520-0493(1982)110<0699:SEITEO>2.0.CO;2.

Nøst, O. A., and P. E. Isachsen, 2003: The large-scale time-mean ocean circulation in the Nordic Seas and Arctic Ocean estimated from simplified dynamics. *J. Mar. Res.*, **61**, 175–210, https://doi.org/10.1357/002224003322005069.

Polyakov, I. V., and Coauthors, 2017: Greater role for Atlantic inflows on sea-ice loss in the Eurasian Basin of the Arctic Ocean. *Science*, **356**, 285–291, https://doi.org/10.1126/science.aai8204.

——, and Coauthors, 2020: Weakening of cold halocline layer exposes sea ice to oceanic heat in the eastern Arctic Ocean. *J. Climate*, **33**, 8107–8123, https://doi.org/10.1175/JCLI-D-19-0976.1.

Proshutinsky, A., and M. Johnson, 1997: Two circulation regimes of the wind-driven Arctic Ocean. *J. Geophys. Res.*, **102**, 12 493–12 514, https://doi.org/10.1029/97JC00738.

——, and Coauthors, 2009: Beaufort Gyre freshwater reservoir: State and variability from observations. *J. Geophys. Res.*, **114**, C00A10, https://doi.org/10.1029/2008JC005104.

——, D. Dukhovskoy, M.-L. Timmermans, R. Krishfield, and J. Bamber, 2015: Arctic circulation regimes. *Philos. Trans. Roy. Soc.*, **373A**, 20140160, https://doi.org/10.1098/rsta.2014.0160.

Quadfasel, D., A. Sy, D. Wells, A. Tunik, M. Tibayrenc, F. Kjellberg, and F. J. Ayala, 1991: Warming in the arctic. *Nature*, **350**, 385, https://doi.org/10.1038/350385a0.

Rabe, B., and Coauthors, 2011: An assessment of Arctic Ocean freshwater content changes from the 1990s to the 2006–2008 period. *Deep-Sea Res. I*, **58**, 173–185, https://doi.org/10.1016/j.dsr.2010.12.002.

Rigor, I. G., and J. M. Wallace, 2004: Variations in the age of Arctic sea-ice and summer sea-ice extent. *Geophys. Res. Lett.*, **31**, L09401, https://doi.org/10.1029/2004GL019492.

——, ——, and R. L. Colony, 2002: Response of sea ice to the Arctic Oscillation. *J. Climate*, **15**, 2648–2663, https://doi.org/10.1175/1520-0442(2002)015<2648:ROSITT>2.0.CO;2.

Rind, D., J. Perlwitz, and P. Lonergan, 2005: AO/NAO response to climate change: 1. Respective influences of stratospheric and tropospheric climate changes. *J. Geophys. Res.*, **110**, D12107, https://doi.org/10.1029/2004JD005103.

Rudels, B., 2012: Arctic Ocean circulation and variability – Advection and external forcing encounter constraints and local processes. *Ocean Sci.*, **8**, 261–286, https://doi.org/10.5194/os-8-261-2012.

——, E. P. Jones, L. G. Anderson, and G. Kattner, 1994: On the intermediate depth waters of the Arctic Ocean. *The Polar Oceans and their Role in Shaping the Global Environment*, *Geophysical Monogr.*, Vol. 85, Amer. Geophys. Union, 33–46.

——, L. G. Anderson, and E. P. Jones, 1996: Formation and evolution of the surface mixed layer and halocline of the Arctic Ocean. *J. Geophys. Res.*, **101**, 8807–8821, https://doi.org/10.1029/96JC00143.

Shindell, D. T., R. L. Miller, G. A. Schmidt, and L. Pandolfo, 1999: Simulation of recent northern winter climate trends by greenhouse-gas forcing. *Nature*, **399**, 452–455, https://doi.org/10.1038/20905.

Smedsrud, L. H., and Coauthors, 2013: The role of the Barents Sea in the Arctic climate system. *Rev. Geophys.*, **51**, 415–449, https://doi.org/10.1002/rog.20017.

——, M. H. Halvorsen, J. C. Stroeve, R. Zhang, and K. Kloster, 2017: Fram Strait sea ice export variability and September Arctic Sea ice extent over the last 80 years. *Cryosphere*, **11**, 65–79, https://doi.org/10.5194/tc-11-65-2017.

Sokolov, A. L., 1962: Drift of ice in the Arctic Basin and changes in ice conditions over the northern sea route (English transl.). *Probl. Arct. Anarct.*, **11**, 1–20.

Spreen, G., L. de Steur, D. Divine, S. Gerland, E. Hansen, and R. Kwok, 2020: Arctic sea ice volume export through Fram Strait from 1992 to 2014. *J. Geophys. Res. Oceans*, **125**, e2019JC016039, https://doi.org/10.1029/2019JC016039.

Steele, M., and T. Boyd, 1998: Retreat of the cold halocline layer in the Arctic Ocean. *J. Geophys. Res.*, **103**, 10 419–10 435, https://doi.org/10.1029/98JC00580.

——, and W. Ermold, 2007: Steric sea level change in the Northern Seas. *J. Climate*, **20**, 403–417, https://doi.org/10.1175/JCLI4022.1.

Swift, J. H., and Coauthors, 1997: Waters of the Makarov and Canada basins. *Deep-Sea Res. II*, **44**, 1503–1529, https://doi.org/10.1016/S0967-0645(97)00055-6.

Thompson, D. W. J., and J. M. Wallace, 1998: The Arctic Oscillation signature in the wintertime geopotential height and temperature fields. *Geophys. Res. Lett.*, **25**, 1297–1300, https://doi.org/10.1029/98GL00950.

——, and ——, 2000: Annular modes in the extratropical circulation. Part I: Month-to-month variability. *J. Climate*, **13**, 1000–1016, https://doi.org/10.1175/1520-0442(2000)013<1000:AMITEC>2.0.CO;2.

——, ——, and G. C. Hegerl, 2000: Annular modes in the extratropical circulation. Part II: Trends. *J. Climate*, **13**, 1018–1036, https://doi.org/10.1175/1520-0442(2000)013<1018:AMITEC>2.0.CO;2.

Thorndike, A. S., and R. Colony, 1982: Sea ice motion in response to geostrophic winds. *J. Geophys. Res.*, **87**, 5845–5852, https://doi.org/10.1029/JC087iC08p05845.

Timmermans, M.-L., and J. Marshall, 2020: Understanding Arctic Ocean circulation: A review of ocean dynamics in a changing climate. *J. Geophys. Res. Oceans*, **125**, e2018JC014378, https://doi.org/10.1029/2018JC014378.

Timokhov, L., and F. Tanis, Eds., 1997a: Environmental Working Group Joint U.S.-Russian Atlas of the Arctic Ocean, version 1. Winter period, National Snow and Ice Data Center, https://doi.org/10.7265/N5H12ZX4.

——, and ——, 1997b: Environmental Working Group Joint U.S.-Russian Atlas of the Arctic Ocean, version 1. Summer period, National Snow and Ice Data Center, https://doi.org/10.7265/N5H12ZX4.

Treshnikov, A. F., 1977: Water masses of the Arctic basin. *Polar Oceans*, M. J. Dunbar, Ed., Arctic Institute of North America, 17–31.

Tucker, W. B., J. W. Weatherly, D. T. Eppler, L. D. Farmer, and D. L. Bentley, 2001: Evidence for rapid thinning of sea ice in the western Arctic Ocean at the end of the 1980s. *Geophys. Res. Lett.*, **28**, 2851–2854, https://doi.org/10.1029/2001GL012967.

Wang, J., and Coauthors, 2009: Is the dipole anomaly a major driver to record lows in Arctic summer sea ice extent? *Geophys. Res. Lett.*, **36**, L05706, https://doi.org/10.1029/2008GL036706.

Williams, J., B. Tremblay, R. Newton, and R. Allard, 2016: Dynamic preconditioning of the minimum September sea-ice extent. *J. Climate*, **29**, 5879–5891, https://doi.org/10.1175/JCLI-D-15-0515.1.

Zhang, J., and M. Steele, 2007: Effect of vertical mixing on the Atlantic water layer circulation in the Arctic Ocean. *J. Geophys. Res.*, **112**, C04S04, https://doi.org/10.1029/2006JC003732.

——, D. Rothrock, and M. Steele, 2000: Recent changes in Arctic Sea ice: The interplay between ice dynamics and thermodynamics. *J. Climate*, **13**, 3099–3114, https://doi.org/10.1175/1520-0442(2000)013<3099:RCIASI>2.0.CO;2.

Zhang, X., M. Ikeda, and J. E. Walsh, 2003: Arctic Sea ice and freshwater changes driven by the atmospheric leading mode in a coupled sea ice–ocean model. *J. Climate*, **16**, 2159–2177, https://doi.org/10.1175/2758.1.

——, J. E. Walsh, J. Zhang, U. S. Bhatt, and M. Ikeda, 2004: Climatology and interannual variability of arctic cyclone activity: 1948–2002. *J. Climate*, **17**, 2300–2317, https://doi.org/10.1175/1520-0442(2004)017<2300:CAIVOA>2.0.CO;2.